SUPG Finite Element Simulations of Compressible Flows for Aerothermodynamic Applications

Benjamin S. Kirk

benjamin.kirk@nasa.gov

Applied Aeroscience & CFD Branch
Aerosciences & Flight Mechanics Division
NASA Lyndon B. Johnson Space Center

March 27, 2007

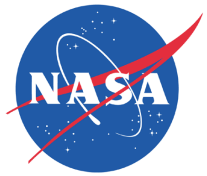

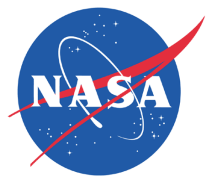

The physical phenomenon of interest is high-speed gas dynamics

Physics

- The compressible Navier-Stokes equations describe fluid flow for *all* Mach numbers
- For aerospace applications of interest the Reynolds number is almost always such that the flows are *convection dominated*
- Multiscale phenomena in the form of shock waves, boundary layers, and shear layers

Numerics

- Discretization of the *conservation law form* of the Navier-Stokes equations is required for convergence to physically valid solutions
- Convective terms must be treated with some form of *upwinding*
- Shocks are treated with some form of *limiting* or *shock capturing*, both of which amount to artificial diffusion which regularizes the problem

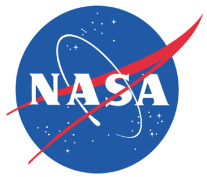

Aerodynamics

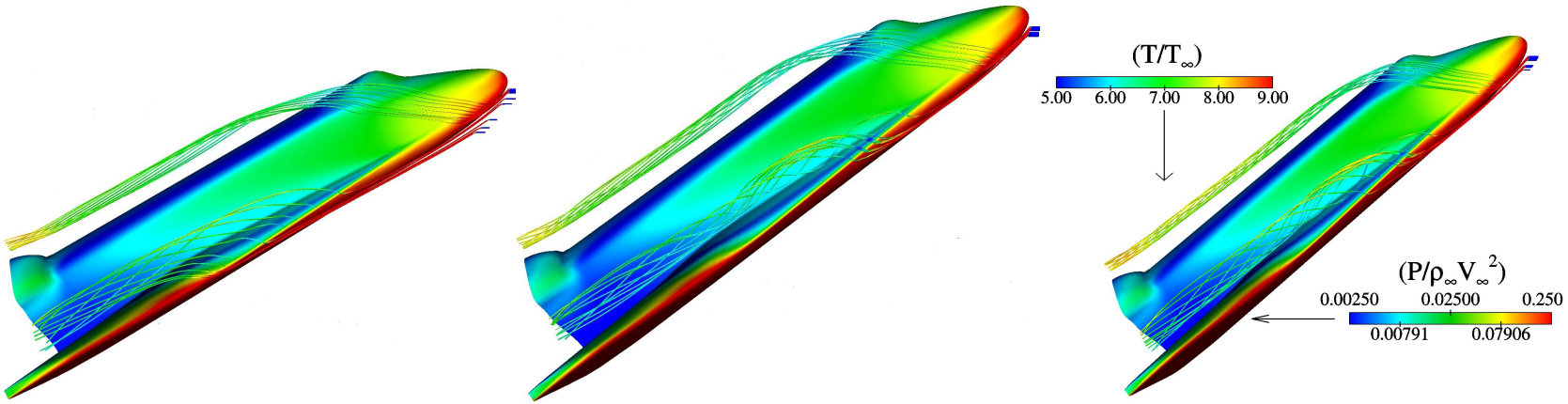

. . . is concerned with predicting aerodynamic forces on a vehicle which result predominantly from the surface pressure distribution, but also from viscous shear stress.

Properly characterizing the aerodynamic performance of reentry vehicles is critical for optimal trajectory design.

Aerothermodynamics

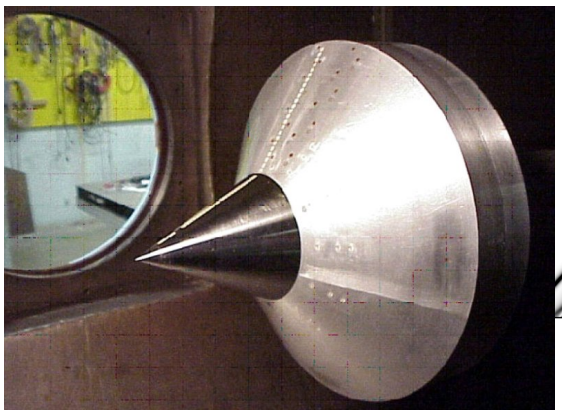

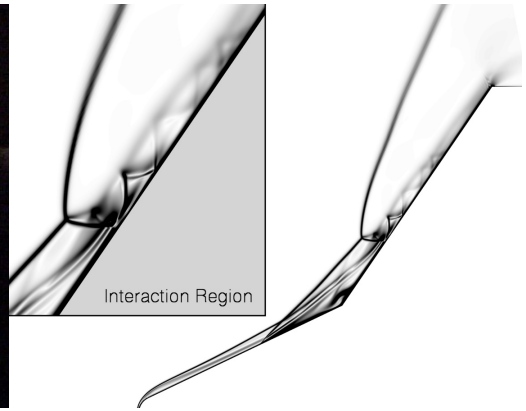

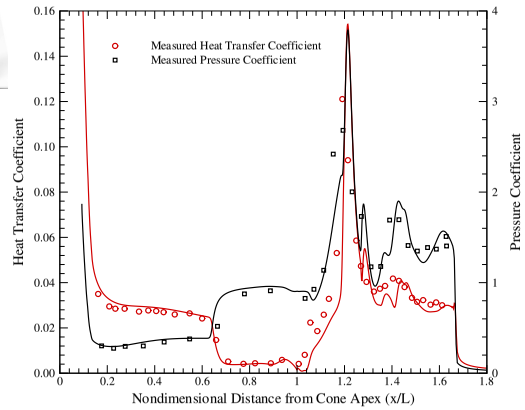

. . . is concerned with predicting the instantaneous total heat transfer rate and integrated heat load into a vehicle.

Properly characterizing this environment is crucial because it provides the design conditions for the thermal protection system:

heat transfer rate → thermal protection material selection
heat load → thermal protection material thickness

The conservation of mass, momentum, and energy for a compressible fluid may be written as

$$\frac{\partial \rho}{\partial t} + \boldsymbol{\nabla} \cdot (\rho \boldsymbol{u}) = 0 \tag{1}$$

$$\frac{\partial \rho \boldsymbol{u}}{\partial t} + \boldsymbol{\nabla} \cdot (\rho \boldsymbol{u}\boldsymbol{u}) = -\boldsymbol{\nabla} P + \boldsymbol{\nabla} \cdot \boldsymbol{\tau} \tag{2}$$

$$\frac{\partial \rho E}{\partial t} + \boldsymbol{\nabla} \cdot (\rho E \boldsymbol{u}) = -\boldsymbol{\nabla} \cdot \boldsymbol{q} - P \boldsymbol{\nabla} \cdot \boldsymbol{u} + \boldsymbol{\nabla} \cdot (\boldsymbol{\tau} \boldsymbol{u}) \tag{3}$$

where ρ is the density, $\boldsymbol{u}$ is the velocity, $E = e + \frac{\boldsymbol{u} \cdot \boldsymbol{u}}{2}$ is the total energy per unit mass, and P is the pressure.

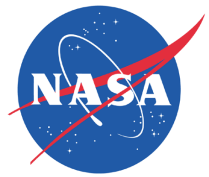

The viscous stress tensor $\boldsymbol{\tau}$ and the heat flux vector $\boldsymbol{q}$ are defined as

$$\boldsymbol{\tau} = \mu\left(\boldsymbol{\nabla u} + \boldsymbol{\nabla}^T \boldsymbol{u}\right) + \lambda\left(\boldsymbol{\nabla} \cdot \boldsymbol{u}\right)\boldsymbol{I} \tag{4}$$

$$\boldsymbol{q} = -k\boldsymbol{\nabla} T \tag{5}$$

where μ is the dynamic viscosity, λ is the second coefficient of viscosity, k is the thermal conductivity, and T is the fluid temperature. The two coefficients of viscosity are related to the bulk viscosity κ by

$$\kappa = \frac{2}{3}\mu + \lambda \tag{6}$$

In general, the bulk viscosity is negligible except in detailed studies of shock wave structure or for investigations of the adsorption and attenuation of acoustic waves [1]. Under this assumption, $\kappa = 0$ in Equation (6) and λ is defined as

$$\lambda = -\frac{2}{3}\mu \tag{7}$$

Equation (4) with (7) is known as Stokes' hypothesis for a Newtonian fluid [2].

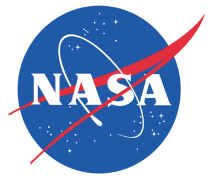

- Provided the transport properties may be related to the unknowns, Equations (1)–(3) form 5 equations in 7 unknowns (in three-dimensions).
- For a gas in thermodynamic equilibrium any two independent properties fix the state:

$$T = T(\rho, e), \quad P = P(\rho, e)$$

- In the special case of a calorically perfect gas

$$c_v T = e, \quad P = \rho e (\gamma - 1)$$

- For the case of thermochemical nonequilibrium the equation set is enlarged to contain
  - local mass balance statements for constituent species
  - local energy balance/exchange statements for internal modes

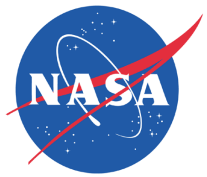

In the literature equations (1)–(3) are often treated as the system[1]

$$\frac{\partial \boldsymbol{U}}{\partial t} + \frac{\partial \boldsymbol{F}_i}{\partial x_i} = \frac{\partial \boldsymbol{G}_i}{\partial x_i} \tag{8}$$

which can be written in terms of the unknowns $\boldsymbol{U} = [\rho, \rho u, \rho v, \rho w, \rho E]^T$ as

$$\frac{\partial \boldsymbol{U}}{\partial t} + \boldsymbol{A}_i \frac{\partial \boldsymbol{U}}{\partial x_i} = \frac{\partial}{\partial x_i}\left(\boldsymbol{K}_{ij}\frac{\partial \boldsymbol{U}}{\partial x_j}\right) \tag{9}$$

where $\boldsymbol{A}_i = \frac{\partial \boldsymbol{F}_i}{\partial \boldsymbol{U}}$ is the inviscid flux Jacobian, and the viscous flux vector $\boldsymbol{G}_i$ may be written as

$$\frac{\partial \boldsymbol{G}_i}{\partial x_i} = \frac{\partial}{\partial x_i}\left(\boldsymbol{K}_{ij}\frac{\partial \boldsymbol{U}}{\partial x_j}\right) \tag{10}$$

[1] the notation is cumbersome, but it is fairly standard

The Streamline-Upwind Petrov-Galerkin Finite Element Method

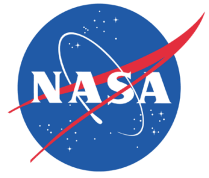

Upwinding is required to stabilize convection-dominated flows. In SUPG schemes this is accomplished by biasing the test functions $\hat{\boldsymbol{W}}$ in the upstream direction:

$$\hat{\boldsymbol{W}} = \boldsymbol{W} + \boldsymbol{\tau}_{SUPG}\, \boldsymbol{A}_i \frac{\partial \boldsymbol{W}}{\partial x_i} \tag{11}$$

Standard Galerkin treatment & SUPG-upwinding applied to (9) to produce the stabilized weak form: *find* $\boldsymbol{U}$ *such that*

$$\int_\Omega \left[\boldsymbol{W} \cdot \left(\frac{\partial \boldsymbol{U}}{\partial t} + \boldsymbol{A}_i \frac{\partial \boldsymbol{U}}{\partial x_i} \right) + \frac{\partial \boldsymbol{W}}{\partial x_i} \cdot \left(\boldsymbol{K}_{ij} \frac{\partial \boldsymbol{U}}{\partial x_j} \right) \right] d\Omega$$

$$+ \sum_{e=1}^{n_{el}} \int_{\Omega_e} \boldsymbol{\tau}_{SUPG} \frac{\partial \boldsymbol{W}}{\partial x_k} \cdot \boldsymbol{A}_k \left[\frac{\partial \boldsymbol{U}}{\partial t} + \boldsymbol{A}_i \frac{\partial \boldsymbol{U}}{\partial x_i} - \frac{\partial}{\partial x_i} \left(\boldsymbol{K}_{ij} \frac{\partial \boldsymbol{U}}{\partial x_j} \right) \right] d\Omega$$

$$= \int_\Gamma \boldsymbol{W} \cdot \boldsymbol{g}\, d\Gamma \tag{12}$$

for all $\boldsymbol{W}$ *in an appropriate function space.*

For compressible flows $\boldsymbol{\tau}_{SUPG}$ is generally diagonal [3].

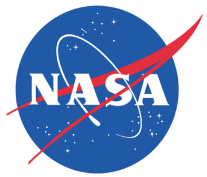

Upwinding is required to stabilize convection-dominated flows. In SUPG schemes this is accomplished by biasing the test functions $\hat{\boldsymbol{W}}$ in the upstream direction:

$$\hat{\boldsymbol{W}} = \boldsymbol{W} + \boldsymbol{\tau}_{SUPG}\, \boldsymbol{A}_i \frac{\partial \boldsymbol{W}}{\partial x_i} \tag{11}$$

Standard Galerkin treatment & SUPG-upwinding applied to (9) to produce the stabilized weak form: *find* $\boldsymbol{U}$ *such that*

$$\int_\Omega \left[\boldsymbol{W} \cdot \left(\frac{\partial \boldsymbol{U}}{\partial t} + \boldsymbol{A}_i \frac{\partial \boldsymbol{U}}{\partial x_i} \right) + \frac{\partial \boldsymbol{W}}{\partial x_i} \cdot \left(\boldsymbol{K}_{ij} \frac{\partial \boldsymbol{U}}{\partial x_j} \right) \right] d\Omega$$

$$+ \sum_{e=1}^{n_{el}} \int_{\Omega_e} \boldsymbol{\tau}_{SUPG} \frac{\partial \boldsymbol{W}}{\partial x_k} \cdot \boldsymbol{A}_k \left[\frac{\partial \boldsymbol{U}}{\partial t} + \boldsymbol{A}_i \frac{\partial \boldsymbol{U}}{\partial x_i} - \frac{\partial}{\partial x_i} \left(\boldsymbol{K}_{ij} \frac{\partial \boldsymbol{U}}{\partial x_j} \right) \right] d\Omega$$

$$= \int_\Gamma \boldsymbol{W} \cdot \boldsymbol{g}\, d\Gamma \tag{12}$$

for all $\boldsymbol{W}$ *in an appropriate function space.*

For compressible flows $\boldsymbol{\tau}_{SUPG}$ is generally diagonal [3].

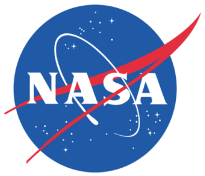

SUPG stabilization does not yield monotone solutions. Additional treatment is needed to prevent spurious oscillations in regions of shockwaves. Hence (12) is augmented with a *shock capturing* term to produce the augmented weak form: *find* $\boldsymbol{U}$ *such that*

$$\int_\Omega \left[\boldsymbol{W} \cdot \left(\frac{\partial \boldsymbol{U}}{\partial t} + \boldsymbol{A}_i \frac{\partial \boldsymbol{U}}{\partial x_i} \right) + \frac{\partial \boldsymbol{W}}{\partial x_i} \cdot \left(\boldsymbol{K}_{ij} \frac{\partial \boldsymbol{U}}{\partial x_j} \right) \right] d\Omega$$

$$+ \sum_{e=1}^{n_{el}} \int_{\Omega_e} \boldsymbol{\tau}_{SUPG} \frac{\partial \boldsymbol{W}}{\partial x_k} \cdot \boldsymbol{A}_k \left[\frac{\partial \boldsymbol{U}}{\partial t} + \boldsymbol{A}_i \frac{\partial \boldsymbol{U}}{\partial x_i} - \frac{\partial}{\partial x_i} \left(\boldsymbol{K}_{ij} \frac{\partial \boldsymbol{U}}{\partial x_j} \right) \right] d\Omega$$

$$+ \sum_{e=1}^{n_{el}} \int_{\Omega_e} \delta \left(\frac{\partial \boldsymbol{W}}{\partial x_i} \cdot \frac{\partial \boldsymbol{U}}{\partial x_i} \right) d\Omega = \int_\Gamma \boldsymbol{W} \cdot \boldsymbol{g} \, d\Gamma \qquad (13)$$

for all $\boldsymbol{W}$ *in an appropriate function space.*

δ in this work is modified from [4, 5]. Note that discretizations of (13) reduce to $\mathcal{O}(h)$ in regions of appreciable δ.

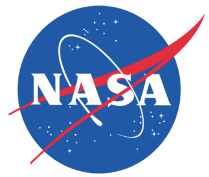

The shock capturing operator, δ, was adapted for a system of conservation variables by LeBeau and Tezduyar [4, 5, 6] from the original definition employed by Hughes et al. for the case of entropy variables [7, 8]. A modified form is employed in the present work and is defined as

$$\delta = \left[\frac{\left\| \frac{\partial \boldsymbol{U}}{\partial t} + \boldsymbol{A}_i \frac{\partial \boldsymbol{U}}{\partial x_i} - \frac{\partial}{\partial x_i}\left(\boldsymbol{K}_{ij} \frac{\partial \boldsymbol{U}}{\partial x_j} \right) \right\|_{\boldsymbol{A}_0^{-1}}}{\|\boldsymbol{\nabla}\xi \cdot \boldsymbol{\nabla}\boldsymbol{U}\|_{\boldsymbol{A}_0^{-1}} + \|\boldsymbol{\nabla}\eta \cdot \boldsymbol{\nabla}\boldsymbol{U}\|_{\boldsymbol{A}_0^{-1}} + \|\boldsymbol{\nabla}\zeta \cdot \boldsymbol{\nabla}\boldsymbol{U}\|_{\boldsymbol{A}_0^{-1}}} \right]^{1/2} \tag{14}$$

where (ξ, η, ζ) are the canonical reference element coordinates and $\boldsymbol{A}_0^{-1}$ is the mapping from conservation to entropy variables.

In this work the numerator is modified from its original form to retain consistency with (9) in the case of transient, viscous flows.

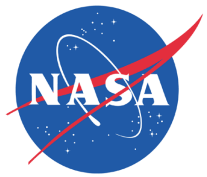

Expand $\boldsymbol{U}(\boldsymbol{x},t)$ and $\boldsymbol{F}_i(\boldsymbol{x},t)$ in terms of standard Lagrange finite element basis functions:

$$\boldsymbol{U}(\boldsymbol{x},t) = \sum_j \phi_j(\boldsymbol{x})\boldsymbol{U}(\boldsymbol{x}_j,t) \tag{15}$$

$$\boldsymbol{F}_i(\boldsymbol{x},t) = \sum_j \phi_j(\boldsymbol{x})\boldsymbol{F}_i(\boldsymbol{x}_j,t) \tag{16}$$

where $\boldsymbol{U}(\boldsymbol{x}_j,t)$ and $\boldsymbol{F}_i(\boldsymbol{x}_j,t) = \boldsymbol{A}_i\left(\boldsymbol{U}\left(\boldsymbol{x}_j,t\right)\right)\boldsymbol{U}(\boldsymbol{x}_j,t)$ are the nodal solution inviscid flux values at time t. A standard piecewise linear Lagrange basis is chosen for $\{\phi\}$ (yielding a nominally 2^{nd}–order accurate scheme).

This approach is in contrast to previous SUPG discretizations for compressible flows. [4, 5, 3, 9]

$$\begin{aligned}\boldsymbol{F}_i(\boldsymbol{x},t) &= \sum_j \phi_j(\boldsymbol{x})\boldsymbol{F}_i(\boldsymbol{x}_j,t) \\ &= \sum_j \phi_j(\boldsymbol{x})\boldsymbol{A}_i\left(\boldsymbol{U}\left(\boldsymbol{x}_j,t\right)\right)\boldsymbol{U}(\boldsymbol{x}_j,t)\end{aligned} \tag{17}$$

contrasts to the typical approach in which

$$\boldsymbol{F}_i(\boldsymbol{x},t) = \boldsymbol{A}_i\left(\boldsymbol{U}\left(\boldsymbol{x},t\right)\right)\boldsymbol{U}(\boldsymbol{x},t) \tag{18}$$

where $\boldsymbol{U}(\boldsymbol{x},t)$ is interpolated from nodal values as in (15).

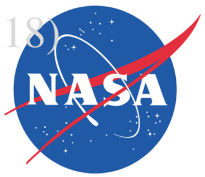

Expand $\boldsymbol{U}(\boldsymbol{x},t)$ and $\boldsymbol{F}_i(\boldsymbol{x},t)$ in terms of standard Lagrange finite element basis functions:

$$\boldsymbol{U}(\boldsymbol{x},t) = \sum_j \phi_j(\boldsymbol{x})\boldsymbol{U}(\boldsymbol{x}_j,t) \tag{15}$$

$$\boldsymbol{F}_i(\boldsymbol{x},t) = \sum_j \phi_j(\boldsymbol{x})\boldsymbol{F}_i(\boldsymbol{x}_j,t) \tag{16}$$

where $\boldsymbol{U}(\boldsymbol{x}_j,t)$ and $\boldsymbol{F}_i(\boldsymbol{x}_j,t) = \boldsymbol{A}_i\left(\boldsymbol{U}\left(\boldsymbol{x}_j,t\right)\right)\boldsymbol{U}(\boldsymbol{x}_j,t)$ are the nodal solution inviscid flux values at time t. A standard piecewise linear Lagrange basis is chosen for $\{\phi\}$ (yielding a nominally 2^{nd}–order accurate scheme).
This approach is in contrast to previous SUPG discretizations for compressible flows. [4, 5, 3, 9]

$$\begin{aligned}\boldsymbol{F}_i(\boldsymbol{x},t) &= \sum_j \phi_j(\boldsymbol{x})\boldsymbol{F}_i(\boldsymbol{x}_j,t) \\ &= \sum_j \phi_j(\boldsymbol{x})\boldsymbol{A}_i\left(\boldsymbol{U}\left(\boldsymbol{x}_j,t\right)\right)\boldsymbol{U}(\boldsymbol{x}_j,t)\end{aligned} \tag{17}$$

contrasts to the typical approach in which

$$\boldsymbol{F}_i(\boldsymbol{x},t) = \boldsymbol{A}_i\left(\boldsymbol{U}\left(\boldsymbol{x},t\right)\right)\boldsymbol{U}(\boldsymbol{x},t) \tag{18}$$

where $\boldsymbol{U}(\boldsymbol{x},t)$ is interpolated from nodal values as in (15).

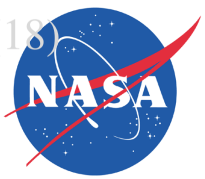

Expand $\boldsymbol{U}(\boldsymbol{x},t)$ and $\boldsymbol{F}_i(\boldsymbol{x},t)$ in terms of standard Lagrange finite element basis functions:

$$\boldsymbol{U}(\boldsymbol{x},t) = \sum_j \phi_j(\boldsymbol{x})\boldsymbol{U}(\boldsymbol{x}_j,t) \tag{15}$$

$$\boldsymbol{F}_i(\boldsymbol{x},t) = \sum_j \phi_j(\boldsymbol{x})\boldsymbol{F}_i(\boldsymbol{x}_j,t) \tag{16}$$

where $\boldsymbol{U}(\boldsymbol{x}_j,t)$ and $\boldsymbol{F}_i(\boldsymbol{x}_j,t) = \boldsymbol{A}_i\left(\boldsymbol{U}\left(\boldsymbol{x}_j,t\right)\right)\boldsymbol{U}(\boldsymbol{x}_j,t)$ are the nodal solution inviscid flux values at time t. A standard piecewise linear Lagrange basis is chosen for $\{\phi\}$ (yielding a nominally 2^{nd}–order accurate scheme).
This approach is in contrast to previous SUPG discretizations for compressible flows. [4, 5, 3, 9]

$$\begin{aligned}\boldsymbol{F}_i(\boldsymbol{x},t) &= \sum_j \phi_j(\boldsymbol{x})\boldsymbol{F}_i(\boldsymbol{x}_j,t) \\ &= \sum_j \phi_j(\boldsymbol{x})\boldsymbol{A}_i\left(\boldsymbol{U}\left(\boldsymbol{x}_j,t\right)\right)\boldsymbol{U}(\boldsymbol{x}_j,t)\end{aligned} \tag{17}$$

contrasts to the typical approach in which

$$\boldsymbol{F}_i(\boldsymbol{x},t) = \boldsymbol{A}_i\left(\boldsymbol{U}\left(\boldsymbol{x},t\right)\right)\boldsymbol{U}(\boldsymbol{x},t) \tag{18}$$

where $\boldsymbol{U}(\boldsymbol{x},t)$ is interpolated from nodal values as in (15).

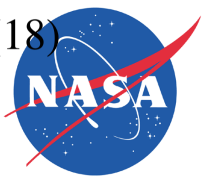

Consider a one-dimensional, inviscid, normal shock at Mach 5. For this simple case the governing equations reduce to

$$\frac{\partial \rho}{\partial t} + \frac{\partial}{\partial x}(\rho u) = 0$$
$$\frac{\partial \rho u}{\partial t} + \frac{\partial}{\partial x}\left(\rho u^2 + P\right) = 0$$
$$\frac{\partial \rho E}{\partial t} + \frac{\partial}{\partial x}(\rho u H) = 0$$

and, at steady state, become

$$\frac{\partial}{\partial x}(\rho u) = \frac{\partial}{\partial x}\left(\rho u^2 + P\right) = \frac{\partial}{\partial x}(\rho u H) \equiv 0 \tag{19}$$

which implies that ρu, $\rho u^2 + P$, and $\rho u H$ are all constant.

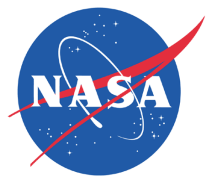

Comparison between reconstructed and interpolated inviscid flux discretizations

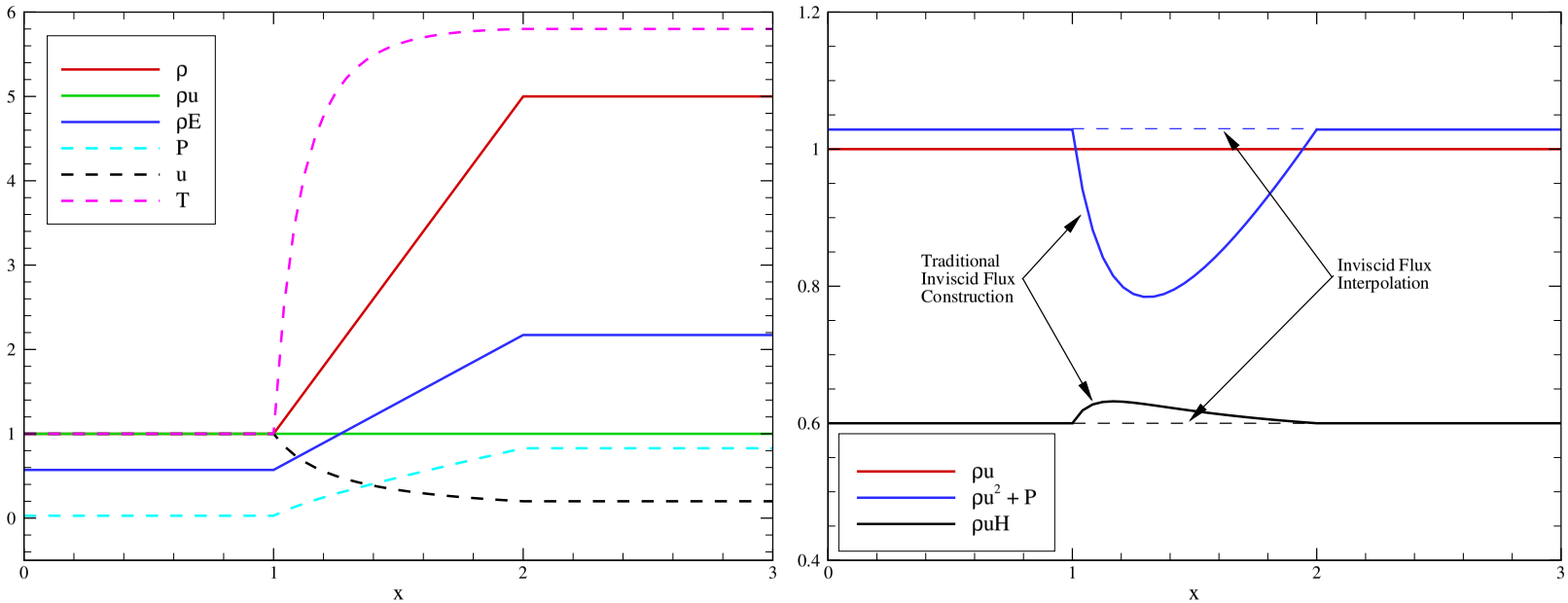

The semidiscrete weak form in equation (13) is discretized in time using a backwards finite difference scheme. Both first and second-order accurate in time schemes may be derived from Taylor series expansions in time about $\boldsymbol{U}_{n+1}$:

$$\boldsymbol{U}_n = \boldsymbol{U}_{n+1} + \frac{\partial \boldsymbol{U}_{n+1}}{\partial t}\left(t_n - t_{n+1}\right) + \frac{\partial^2 \boldsymbol{U}_{n+1}}{\partial t^2}\frac{\left(t_n - t_{n+1}\right)^2}{2} + \mathcal{O}\left(\left(t_n - t_{n+1}\right)^3\right)$$

$$\boldsymbol{U}_{n-1} = \boldsymbol{U}_{n+1} + \frac{\partial \boldsymbol{U}_{n+1}}{\partial t}\left(t_{n-1} - t_{n+1}\right) + \frac{\partial^2 \boldsymbol{U}_{n+1}}{\partial t^2}\frac{\left(t_{n-1} - t_{n+1}\right)^2}{2} + \mathcal{O}\left(\left(t_{n-1} - t_{n+1}\right)^3\right)$$

which, upon substituting $t_{n+1} - t_n \equiv \Delta t_{n+1}$ and $t_{n+1} - t_{n-1} = \Delta t_{n+1} + \Delta t_n$, becomes

$$\boldsymbol{U}_n = \boldsymbol{U}_{n+1} - \frac{\partial \boldsymbol{U}_{n+1}}{\partial t}\Delta t_{n+1} + \frac{\partial^2 \boldsymbol{U}_{n+1}}{\partial t^2}\frac{\Delta t_{n+1}^2}{2} - \mathcal{O}\left(\Delta t_{n+1}^3\right)$$

$$\boldsymbol{U}_{n-1} = \boldsymbol{U}_{n+1} - \frac{\partial \boldsymbol{U}_{n+1}}{\partial t}\left(\Delta t_{n+1} + \Delta t_n\right) + \frac{\partial^2 \boldsymbol{U}_{n+1}}{\partial t^2}\frac{\left(\Delta t_{n+1} + \Delta t_n\right)^2}{2} - \mathcal{O}\left(\left(\Delta t_{n+1} + \Delta t_n\right)^3\right)$$

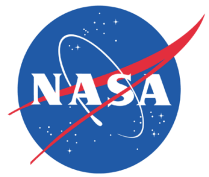

The semidiscrete weak form in equation (13) is discretized in time using a backwards finite difference scheme. Both first and second-order accurate in time schemes may be derived from Taylor series expansions in time about $\boldsymbol{U}_{n+1}$:

$$\boldsymbol{U}_n = \boldsymbol{U}_{n+1} + \frac{\partial \boldsymbol{U}_{n+1}}{\partial t}\left(t_n - t_{n+1}\right) + \frac{\partial^2 \boldsymbol{U}_{n+1}}{\partial t^2}\frac{\left(t_n - t_{n+1}\right)^2}{2} + \mathcal{O}\left(\left(t_n - t_{n+1}\right)^3\right)$$

$$\boldsymbol{U}_{n-1} = \boldsymbol{U}_{n+1} + \frac{\partial \boldsymbol{U}_{n+1}}{\partial t}\left(t_{n-1} - t_{n+1}\right) + \frac{\partial^2 \boldsymbol{U}_{n+1}}{\partial t^2}\frac{\left(t_{n-1} - t_{n+1}\right)^2}{2} + \mathcal{O}\left(\left(t_{n-1} - t_{n+1}\right)^3\right)$$

which, upon substituting $t_{n+1} - t_n \equiv \Delta t_{n+1}$ and $t_{n+1} - t_{n-1} = \Delta t_{n+1} + \Delta t_n$, becomes

$$\boldsymbol{U}_n = \boldsymbol{U}_{n+1} - \frac{\partial \boldsymbol{U}_{n+1}}{\partial t}\Delta t_{n+1} + \frac{\partial^2 \boldsymbol{U}_{n+1}}{\partial t^2}\frac{\Delta t_{n+1}^2}{2} - \mathcal{O}\left(\Delta t_{n+1}^3\right)$$

$$\boldsymbol{U}_{n-1} = \boldsymbol{U}_{n+1} - \frac{\partial \boldsymbol{U}_{n+1}}{\partial t}\left(\Delta t_{n+1} + \Delta t_n\right) + \frac{\partial^2 \boldsymbol{U}_{n+1}}{\partial t^2}\frac{\left(\Delta t_{n+1} + \Delta t_n\right)^2}{2} - \mathcal{O}\left(\left(\Delta t_{n+1} + \Delta t_n\right)^3\right)$$

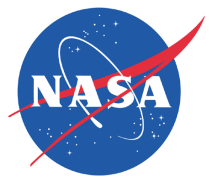

The semidiscrete weak form in equation (13) is discretized in time using a backwards finite difference scheme. Both first and second-order accurate in time schemes may be derived from Taylor series expansions in time about $\boldsymbol{U}_{n+1}$:

$$\boldsymbol{U}_n = \boldsymbol{U}_{n+1} + \frac{\partial \boldsymbol{U}_{n+1}}{\partial t}\left(t_n - t_{n+1}\right) + \frac{\partial^2 \boldsymbol{U}_{n+1}}{\partial t^2}\frac{\left(t_n - t_{n+1}\right)^2}{2} + \mathcal{O}\left(\left(t_n - t_{n+1}\right)^3\right)$$

$$\boldsymbol{U}_{n-1} = \boldsymbol{U}_{n+1} + \frac{\partial \boldsymbol{U}_{n+1}}{\partial t}\left(t_{n-1} - t_{n+1}\right) + \frac{\partial^2 \boldsymbol{U}_{n+1}}{\partial t^2}\frac{\left(t_{n-1} - t_{n+1}\right)^2}{2} + \mathcal{O}\left(\left(t_{n-1} - t_{n+1}\right)^3\right)$$

which, upon substituting $t_{n+1} - t_n \equiv \Delta t_{n+1}$ and $t_{n+1} - t_{n-1} = \Delta t_{n+1} + \Delta t_n$, becomes

$$\boldsymbol{U}_n = \boldsymbol{U}_{n+1} - \frac{\partial \boldsymbol{U}_{n+1}}{\partial t}\Delta t_{n+1} + \frac{\partial^2 \boldsymbol{U}_{n+1}}{\partial t^2}\frac{\Delta t_{n+1}^2}{2} - \mathcal{O}\left(\Delta t_{n+1}^3\right)$$

$$\boldsymbol{U}_{n-1} = \boldsymbol{U}_{n+1} - \frac{\partial \boldsymbol{U}_{n+1}}{\partial t}\left(\Delta t_{n+1} + \Delta t_n\right) + \frac{\partial^2 \boldsymbol{U}_{n+1}}{\partial t^2}\frac{\left(\Delta t_{n+1} + \Delta t_n\right)^2}{2} - \mathcal{O}\left(\left(\Delta t_{n+1} + \Delta t_n\right)^3\right)$$

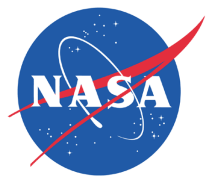

Which can be rewritten for $\frac{\partial \boldsymbol{U}_{n+1}}{\partial t}$ as:

$$\frac{\partial \boldsymbol{U}_{n+1}}{\partial t} = \frac{\boldsymbol{U}_{n+1}}{\Delta t_{n+1}} - \frac{\boldsymbol{U}_{n}}{\Delta t_{n+1}} + \frac{\partial^2 \boldsymbol{U}_{n+1}}{\partial t^2}\frac{\Delta t_{n+1}}{2} - \mathcal{O}\left(\Delta t_{n+1}^2\right) \tag{20}$$

$$\frac{\partial \boldsymbol{U}_{n+1}}{\partial t} = \frac{\boldsymbol{U}_{n+1}}{\Delta t_{n+1} + \Delta t_n} - \frac{\boldsymbol{U}_{n-1}}{\Delta t_{n+1} + \Delta t_n} + \frac{\partial^2 \boldsymbol{U}_{n+1}}{\partial t^2}\frac{(\Delta t_{n+1} + \Delta t_n)}{2} - \mathcal{O}\left((\Delta t_{n+1} + \Delta t_n)^2\right) \tag{21}$$

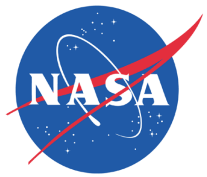

The familiar backwards Euler time discretization follows directly from (20) by recognizing

$$\frac{\partial \boldsymbol{U}_{n+1}}{\partial t} = \frac{\boldsymbol{U}_{n+1} - \boldsymbol{U}_n}{\Delta t_{n+1}} + \mathcal{O}\left(\Delta t_{n+1}\right) \tag{22}$$

which provides a first-order in time approximation upon neglecting the $\mathcal{O}\left(\Delta t_{n+1}\right)$ term.

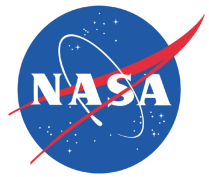

A linear combination of $\left(1+\frac{\Delta t_{n+1}}{\Delta t_n}\right)\times(20)$ and $-\frac{\Delta t_{n+1}}{\Delta t_n}\times(21)$ can be used to annihilate the leading $\frac{\partial^2 \boldsymbol{U}_{n+1}}{\partial t^2}$ term to create a backwards, second-order accurate approximation to $\frac{\partial \boldsymbol{U}_{n+1}}{\partial t}$. This approximation, along with (22), can be generalized in the form

$$\frac{\partial \boldsymbol{U}_{n+1}}{\partial t} = \alpha_t \boldsymbol{U}_{n+1} + \beta_t \boldsymbol{U}_n + \gamma_t \boldsymbol{U}_{n-1} + \mathcal{O}\left(\Delta t_{n+1}^p\right) \tag{23}$$

to yield either a first or second-order accurate scheme. The weights α_t, β_t, and γ_t are given below for $p=1$ and $p=2$.

p	α_t	β_t	γ_t
1	$\frac{1}{\Delta t_{n+1}}$	$\frac{-1}{\Delta t_{n+1}}$	0
2	$-\beta_t-\gamma_t$	$-\left[\frac{1}{\Delta t_{n+1}}+\frac{1}{\Delta t_n}\right]$	$\frac{\Delta t_{n+1}}{\Delta t_n(\Delta t_{n+1}+\Delta t_n)}$

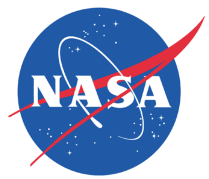

Time Step Selection

The simulation begins with the domain initialized to freestream conditions everywhere and a user-specified initial time step Δt_0 is used to advance the solution. The time step then grows geometrically with the relative change in the unsteady residual measured over k time steps. Explicitly,

$$\Delta \bar{t}_{n+1} = \Delta t_{n-k} \max \left(\left[\frac{\mathcal{R}_{n-k}}{\mathcal{R}_n} \right]^r, 1 \right) \tag{24}$$

$$\Delta t_{n+1} = \min \left(\Delta \bar{t}_{n+1}, \Delta t_{\max} \right) \tag{25}$$

where $\mathcal{R}_n \equiv \left\| \frac{\Delta \boldsymbol{U}_n}{\Delta t} \right\|_\infty$ and $r = 1.2$ is the geometric growth rate. The time step size is updated every $k = 5$ time steps.

Typically the maximum allowable time step for steady problems is $\Delta t_{\max} = 1$, which corresponds to the amount of time required for a fictitious point in the freestream to be convected one reference length.

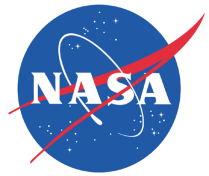

After temporal & spatial discretization, Equation (13) can be written in residual form for the unknown nodal values $\boldsymbol{U}_{n+1} \equiv \boldsymbol{U}_h\left(t_{n+1}\right)$ as the nonlinear algebraic system

$$\boldsymbol{R}\left(\boldsymbol{U}_{n+1}\right) = 0 \tag{26}$$

We seek to define a sequence of linear problems $\left\{\boldsymbol{U}_{n+1}^{l}\right\}$ that converge to $\boldsymbol{U}_{n+1}$, the solution of (26).

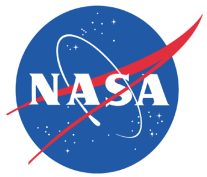

Newton Scheme

Expanding (26) with a Taylor series about iterate $\boldsymbol{U}_{n+1}^{l}$ gives

$$\boldsymbol{R}\left(\boldsymbol{U}_{n+1}^{l+1}\right) = \boldsymbol{R}\left(\boldsymbol{U}_{n+1}^{l}\right) + \left[\frac{\partial \boldsymbol{R}\left(\boldsymbol{U}_{n+1}^{l}\right)}{\partial \boldsymbol{U}_{n+1}}\right] \delta \boldsymbol{U}_{n+1}^{l+1} + \mathcal{O}\left(\left(\delta \boldsymbol{U}_{n+1}^{l+1}\right)^{2}\right) \tag{27}$$

where $\frac{\partial \boldsymbol{R}}{\partial \boldsymbol{U}}$ is the Jacobian matrix for the nonlinear system and $\delta \boldsymbol{U}_{n+1}^{l+1} = \boldsymbol{U}_{n+1}^{l+1} - \boldsymbol{U}_{n+1}^{l}$.

Truncating this expansion and setting $\boldsymbol{R}\left(\boldsymbol{U}_{n+1}^{l+1}\right) = 0$ yields Newton's method:

$$0 = \boldsymbol{R}\left(\boldsymbol{U}_{n+1}^{l}\right) + \left[\frac{\partial \boldsymbol{R}\left(\boldsymbol{U}_{n+1}^{l}\right)}{\partial \boldsymbol{U}_{n+1}}\right] \delta \boldsymbol{U}_{n+1}^{l+1}$$

$$\left[\frac{\partial \boldsymbol{R}\left(\boldsymbol{U}_{n+1}^{l}\right)}{\partial \boldsymbol{U}_{n+1}}\right] \delta \boldsymbol{U}_{n+1}^{l+1} = -\boldsymbol{R}\left(\boldsymbol{U}_{n+1}^{l}\right) \tag{28}$$

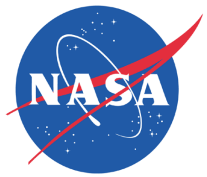

Newton Scheme

Expanding (26) with a Taylor series about iterate $\boldsymbol{U}_{n+1}^{l}$ gives

$$\boldsymbol{R}\left(\boldsymbol{U}_{n+1}^{l+1}\right)=\boldsymbol{R}\left(\boldsymbol{U}_{n+1}^{l}\right)+\left[\frac{\partial \boldsymbol{R}\left(\boldsymbol{U}_{n+1}^{l}\right)}{\partial \boldsymbol{U}_{n+1}}\right]\delta \boldsymbol{U}_{n+1}^{l+1}+\mathcal{O}\left(\left(\delta \boldsymbol{U}_{n+1}^{l+1}\right)^{2}\right) \tag{27}$$

where $\frac{\partial \boldsymbol{R}}{\partial \boldsymbol{U}}$ is the Jacobian matrix for the nonlinear system and $\delta \boldsymbol{U}_{n+1}^{l+1}=\boldsymbol{U}_{n+1}^{l+1}-\boldsymbol{U}_{n+1}^{l}$.

Truncating this expansion and setting $\boldsymbol{R}\left(\boldsymbol{U}_{n+1}^{l+1}\right)=0$ yields Newton's method:

$$0=\boldsymbol{R}\left(\boldsymbol{U}_{n+1}^{l}\right)+\left[\frac{\partial \boldsymbol{R}\left(\boldsymbol{U}_{n+1}^{l}\right)}{\partial \boldsymbol{U}_{n+1}}\right]\delta \boldsymbol{U}_{n+1}^{l+1}$$

$$\left[\frac{\partial \boldsymbol{R}\left(\boldsymbol{U}_{n+1}^{l}\right)}{\partial \boldsymbol{U}_{n+1}}\right]\delta \boldsymbol{U}_{n+1}^{l+1}=-\boldsymbol{R}\left(\boldsymbol{U}_{n+1}^{l}\right) \tag{28}$$

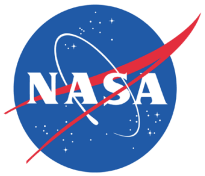

Newton Scheme – Comments

- Newton's method exhibits second-order *conditional* convergence
- Even for a calorically perfect gas, full Newton implementation is complicated by the nonlinear transport properties and convective terms
- Asymptotic convergence rate is rarely achieved for flows with strong shocks
- Computational cost of full-Newton may be mitigated with an approximate Newton-Krylov technique which accounts for the action of the Jacobian matrix in (28) without explicitly forming it
- This approach is especially attractive for "real gas" flows

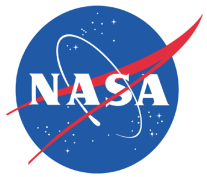

Newton-Krylov Techniques

- The resulting sparse implicit linear systems are amenable to solution with iterative Krylov subspace techniques
- The kernel operation for such methods is the *action* of a matrix-vector product. That is, solving

$$\boldsymbol{K}\boldsymbol{u} = \boldsymbol{f}$$

  requires repeated computations of $\boldsymbol{w} = \boldsymbol{K}\boldsymbol{v}$
- For the Newton linearization,

$$\left[\frac{\partial \boldsymbol{R}}{\partial \boldsymbol{U}}\right] \delta \boldsymbol{U} = -\boldsymbol{R}(\boldsymbol{U})$$

  and the required matrix-vector product is of the form $\boldsymbol{w} = \left[\frac{\partial \boldsymbol{R}}{\partial \boldsymbol{U}}\right] \boldsymbol{v}$, which is simply the derivative of $\boldsymbol{R}$ in the direction of $\boldsymbol{v}$
- This may be approximated via differencing residual evaluations, yielding a so-called matrix-free method:

$$\boldsymbol{w} = \left[\frac{\partial \boldsymbol{R}}{\partial \boldsymbol{U}}\right] \boldsymbol{v} \approx \frac{\boldsymbol{R}(\boldsymbol{U} + \varepsilon \boldsymbol{v}) - \boldsymbol{R}(\boldsymbol{U})}{\varepsilon}$$

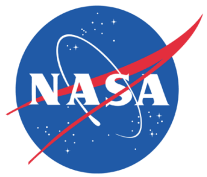

- Time-marching to steady-state is almost always used for high-speed flows
- Implicit techniques required for viscous problems with tight wall spacing (also for stiff chemistry in the case of nonequilibrium)
- For steady problems, at each time step the resulting nonlinear problem is usually solved only approximately (usually 1 Newton step)
- DOF coupling defined via standard finite element basis function support determines sparse matrix structure
- Matrix-free GMRES with block-diagonal preconditioning used in earlier work [5]
- This work uses matrix & matrix-free GMRES with full ILU-0 preconditioning – *linearization is important*

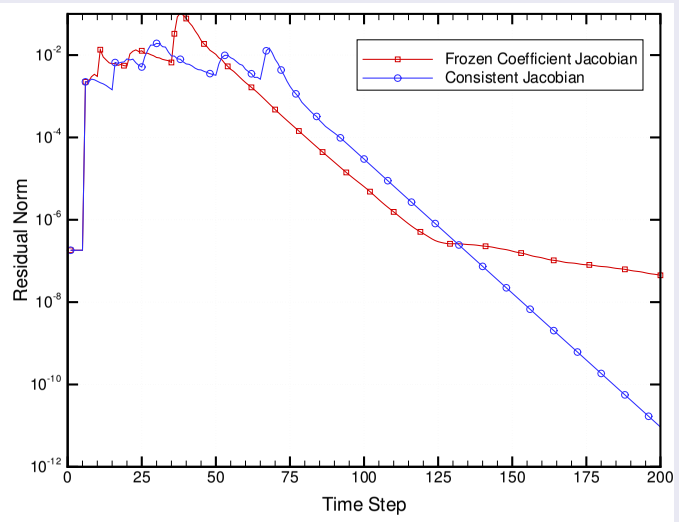

Influence of linearization strategy on iterative convergence for Mach 3 flow over a cylinder

Hypersonic Aerothermodynamics – Application Studies

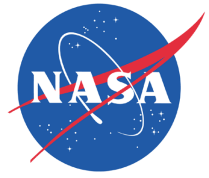

The X-15 Experience

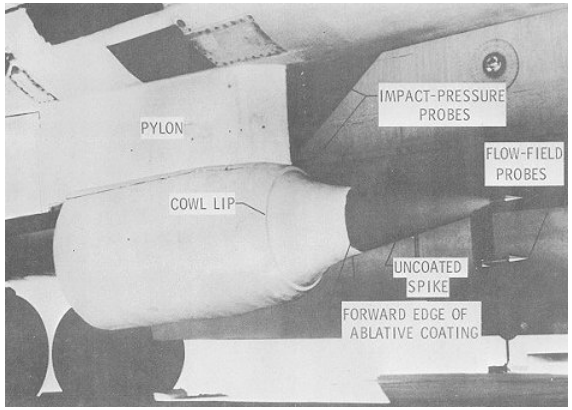

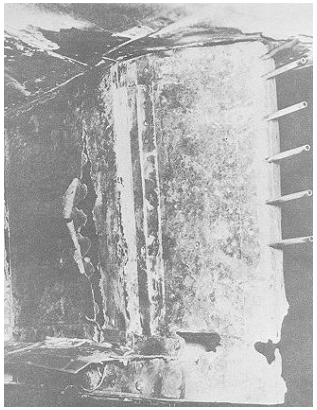

Edney's Type IV Interaction Pattern [10]

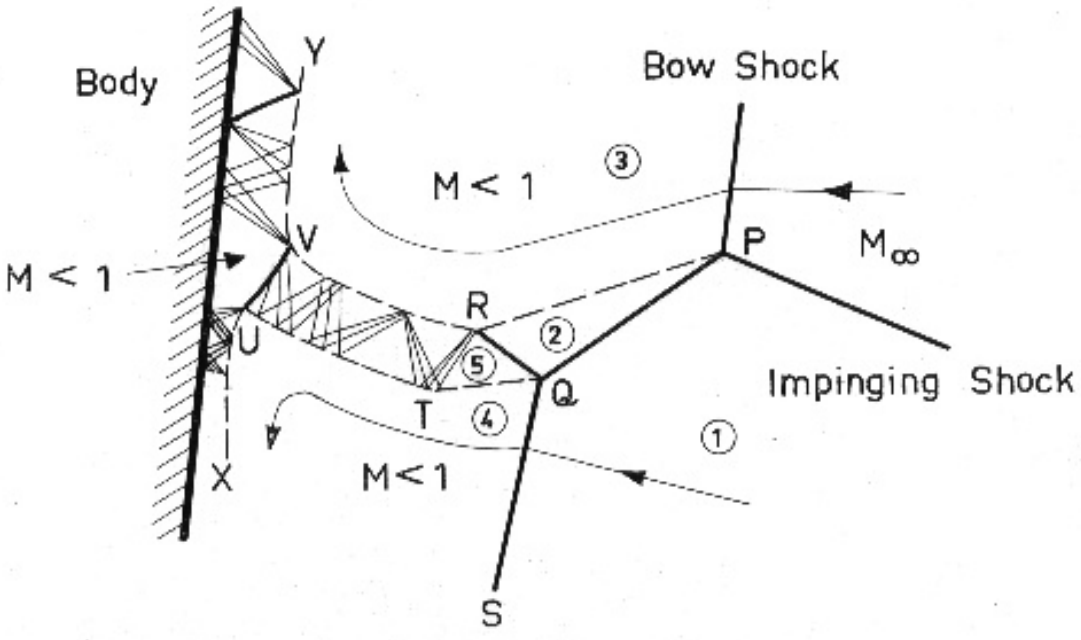

WEDGE

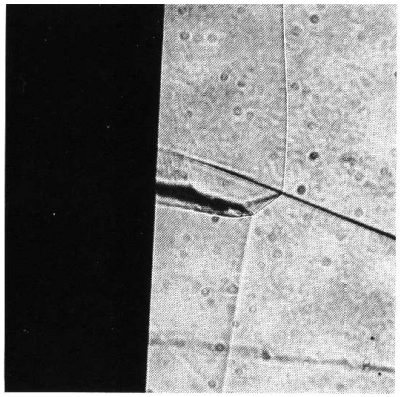

SWEPT CYLINDER

An experimental test program was conducted in 1998 by France's Office National d'Etudes et de Recherches Aérospatiales (ONERA) to investigate shock-shock interactions produced by an oblique shock impinging on the bow shock of a cylinder [11]. This configuration is examined here to assess the quality of surface heat transfer predictions.

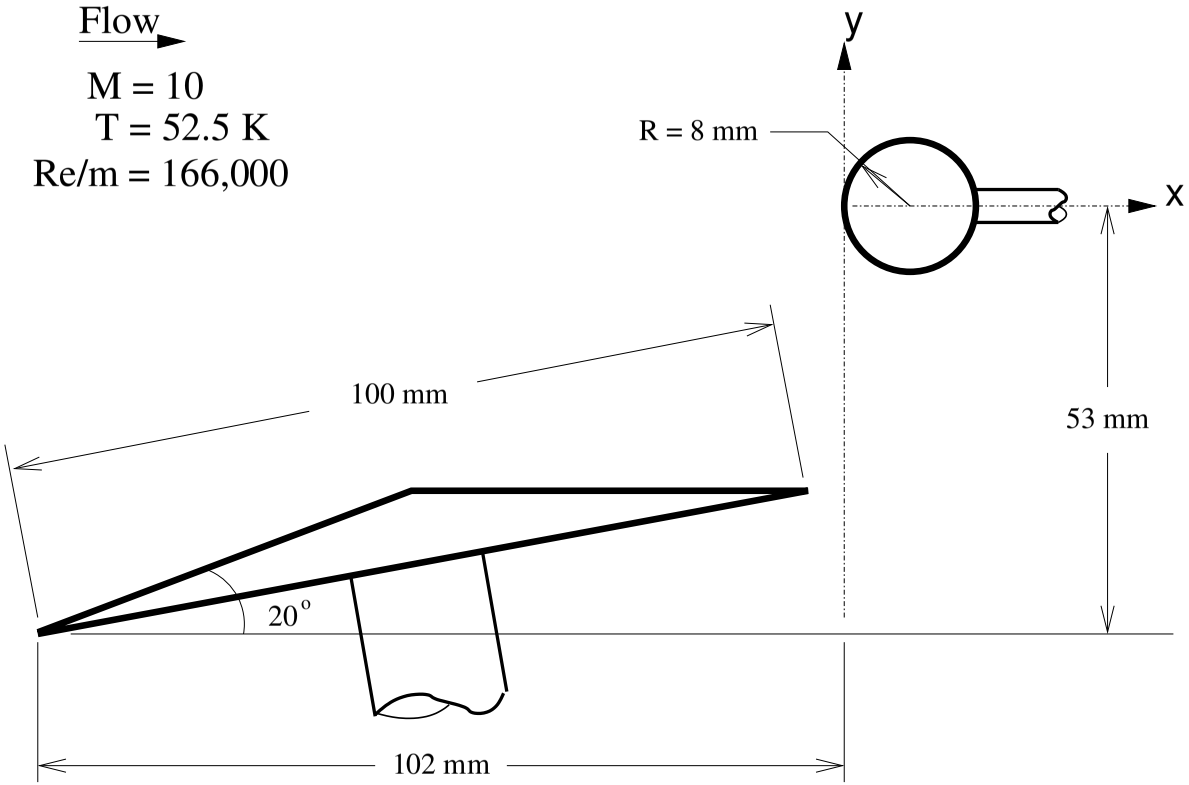

Static temperature contours

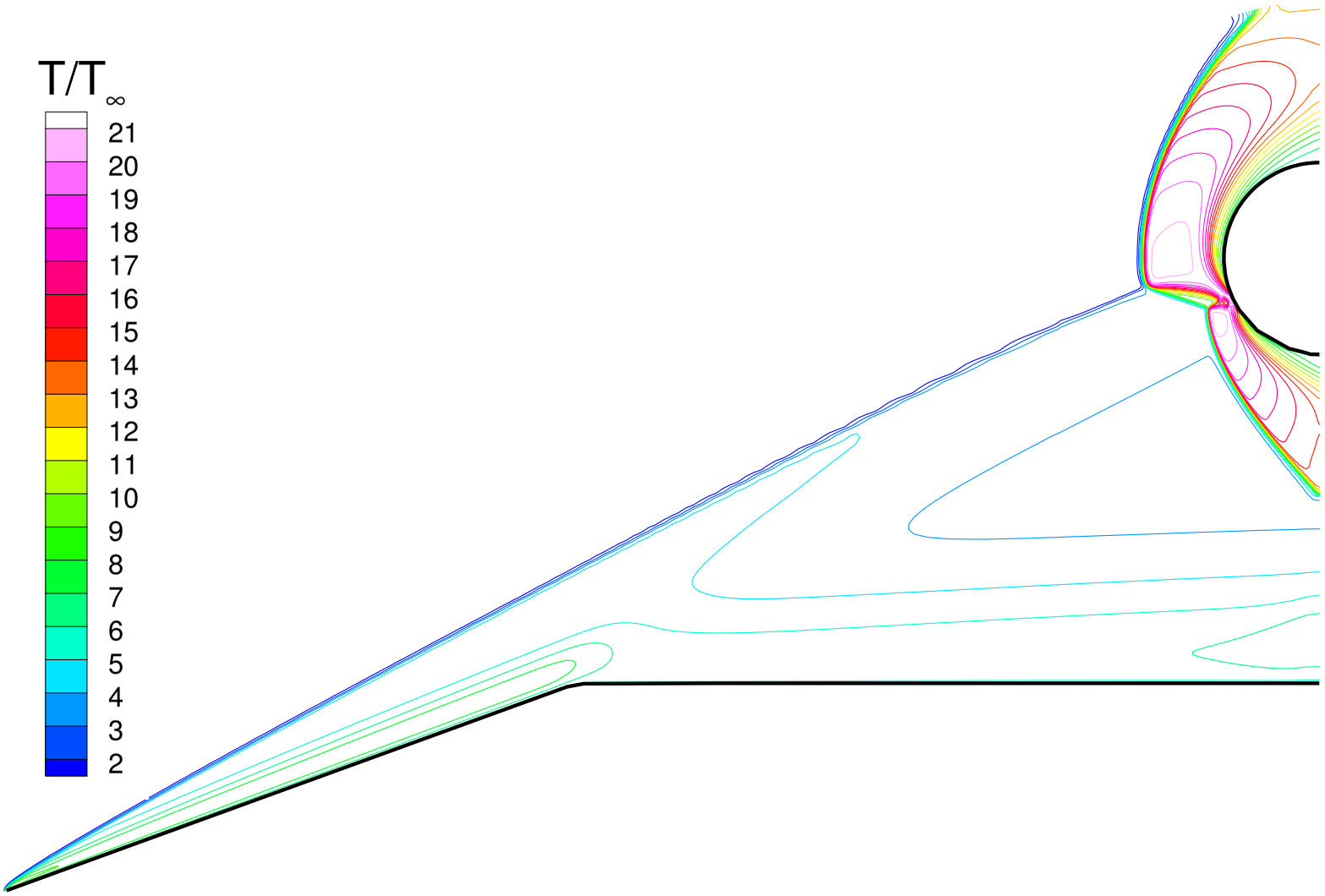

Type IV Shock Interaction

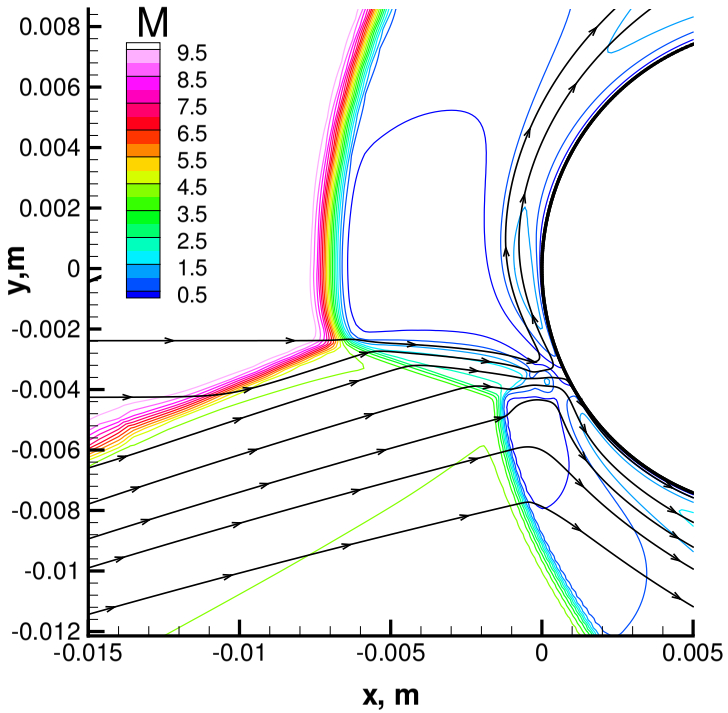

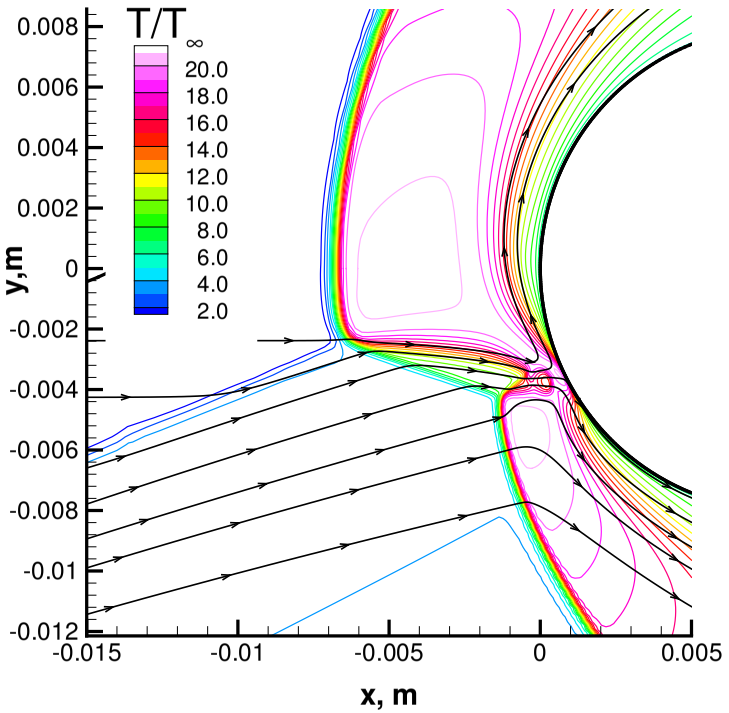

Type IV Shock Interaction

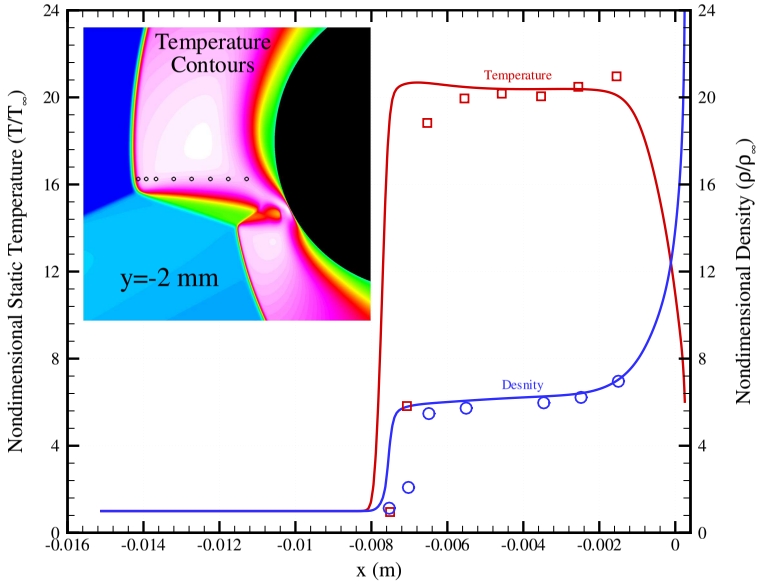

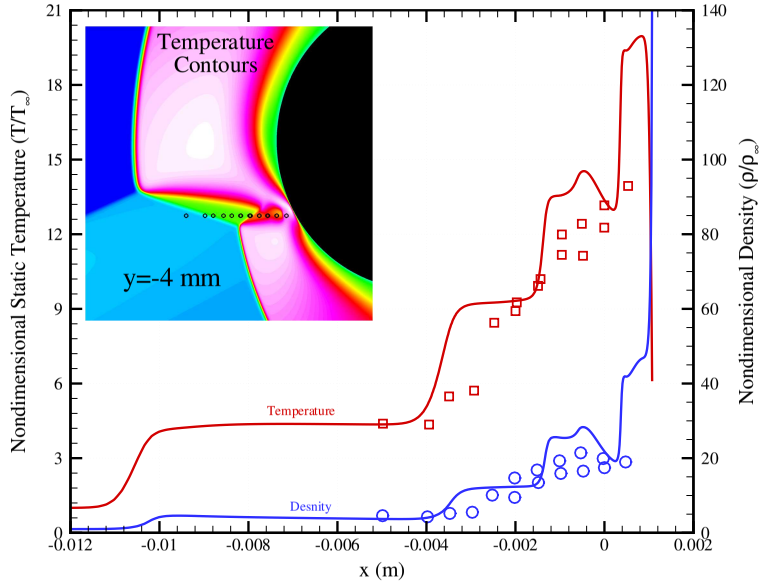

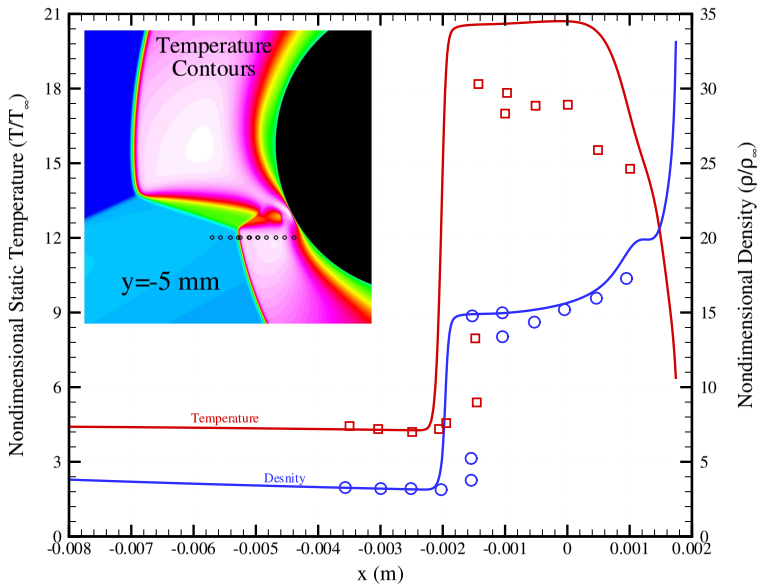

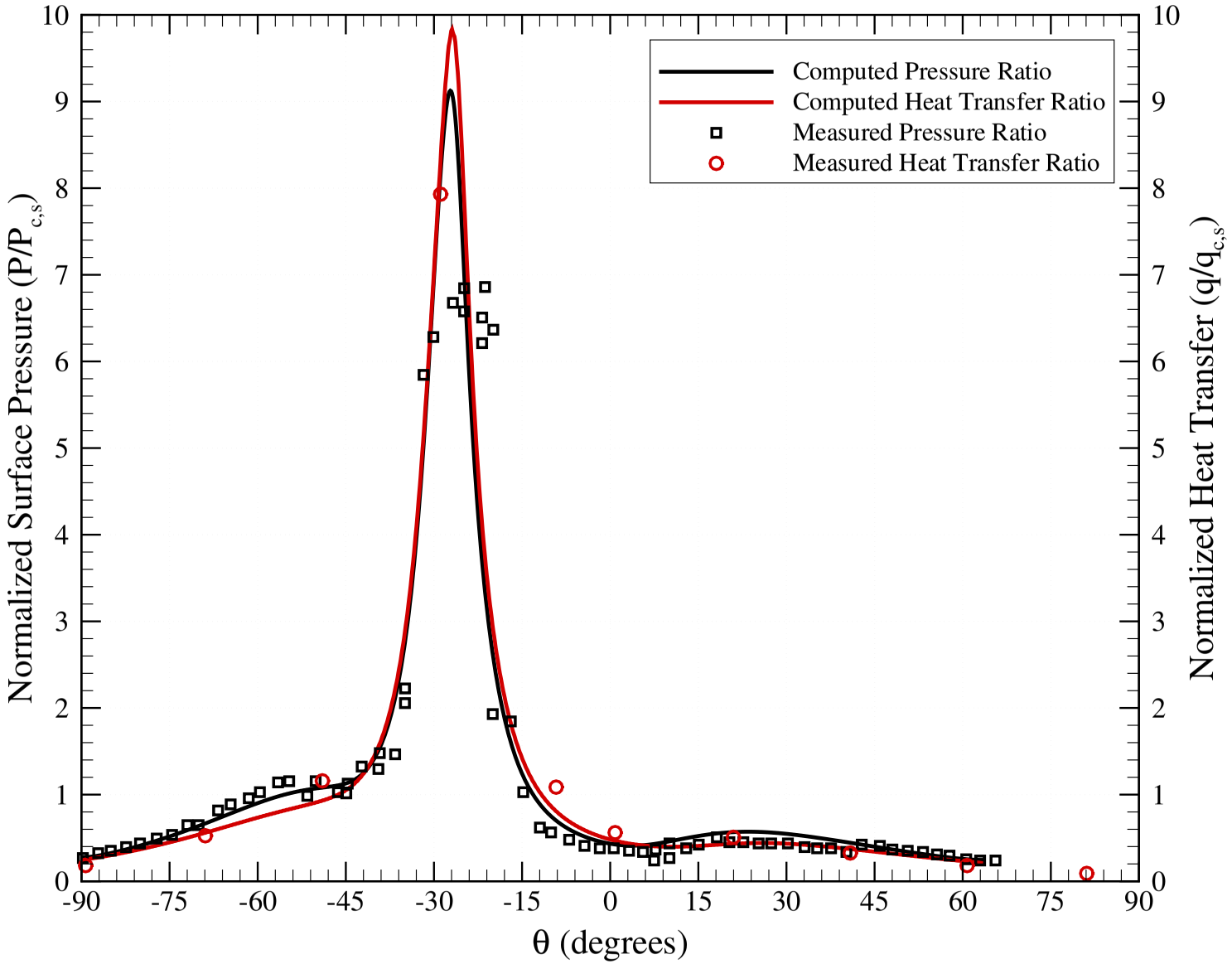
Computed Pressure Ratio
Computed Heat Transfer Ratio
Measured Pressure Ratio
Measured Heat Transfer Ratio
Normalized Surface Pressure (P/P c,s)
Normalized Heat Transfer (q/q c,s)
θ (degrees)
10
9
8
7
6
5
4
3
2
1
0
-90
-75
-60
-45
-30
-15
0
15
30
45
60
75
90

Hypersonic flow over a missile nose tip with a forward facing cavity has been observed to exhibit transient flowfield response in both experimental investigations and numerical simulations [12, 13]. The flowfield response characteristics are largely driven by the cavity length-to-diameter ratio (L/D).

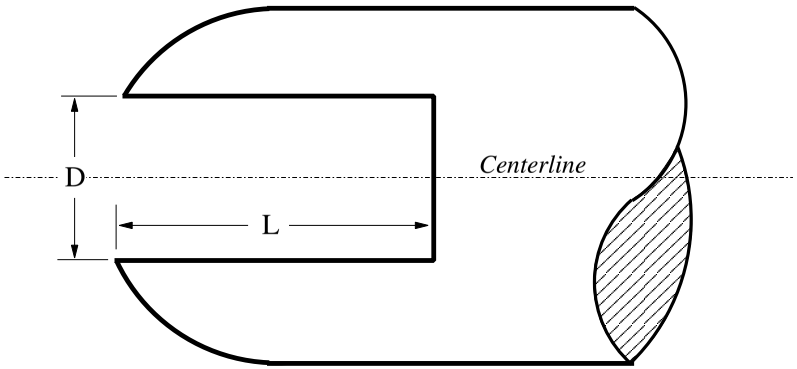

Experimental studies in conventional tunnels report oscillatory response even for relatively shallow cavities, suggesting a threshold L/D of 0.4. Numerical simulations predict a higher threshold L/D of ≈ 1.25. Subsequent studies in a quiet wind tunnel verify the computational results, indicating freestream noise is the mechanism for driving unsteady response in shallow cavities [14].

Forward-Facing Cavity

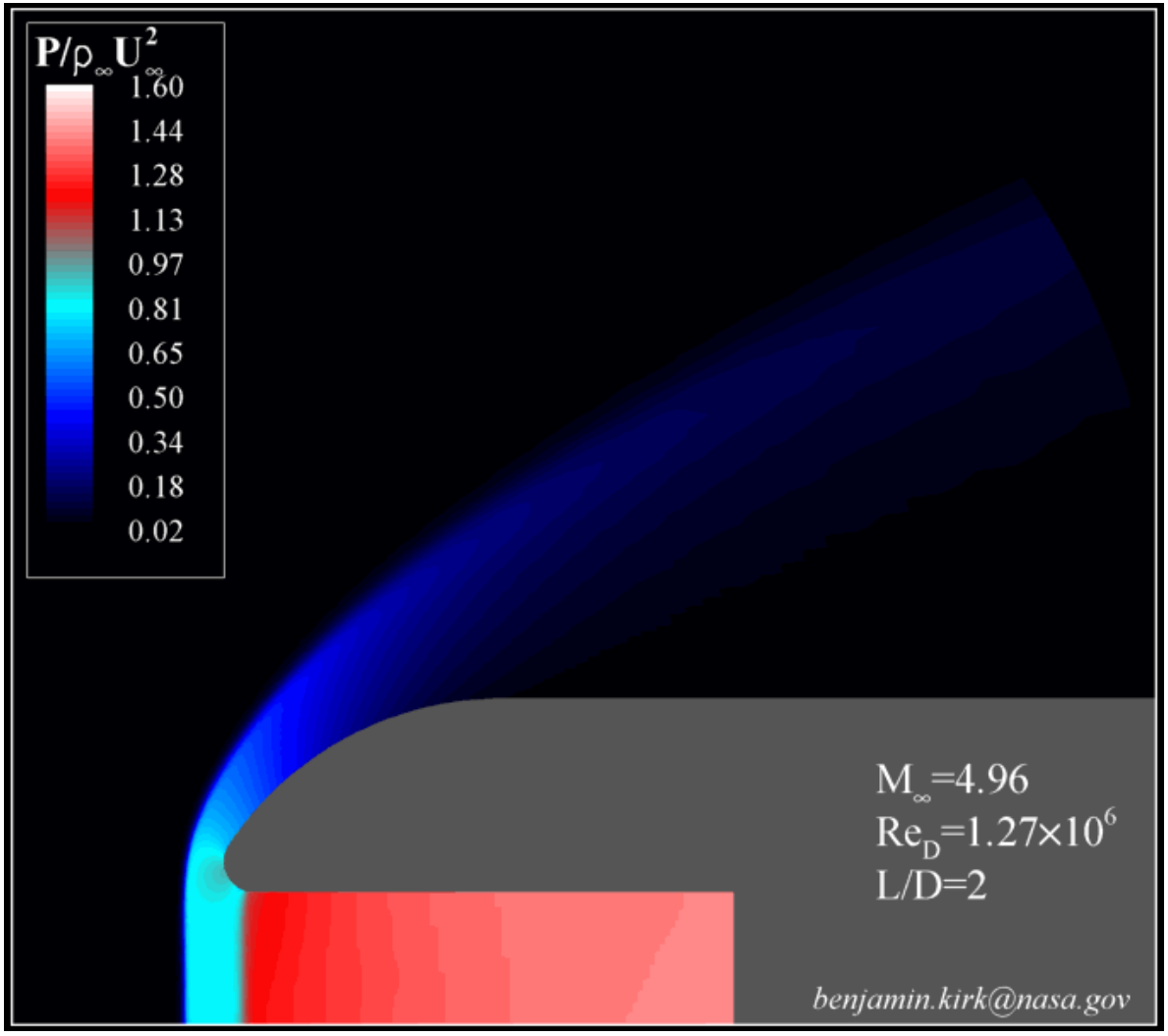

Forward-Facing Cavity

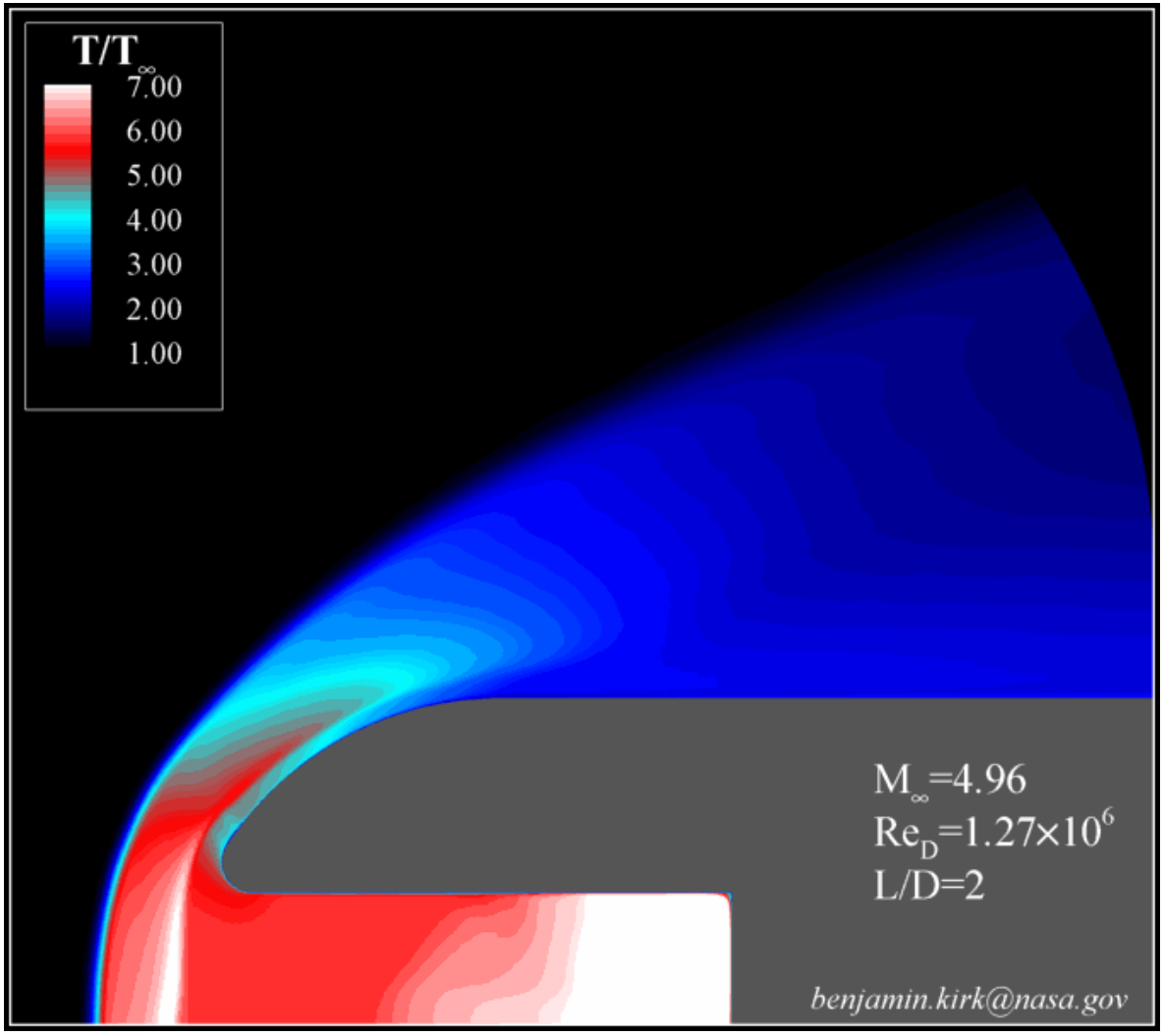

Cavity base pressure versus time for a series of simulations used to assess time convergence.
For $\mathrm{CFL}_{\max} = 20 \times 10^3$ there are ≈ 200 time steps per oscillation cycle.

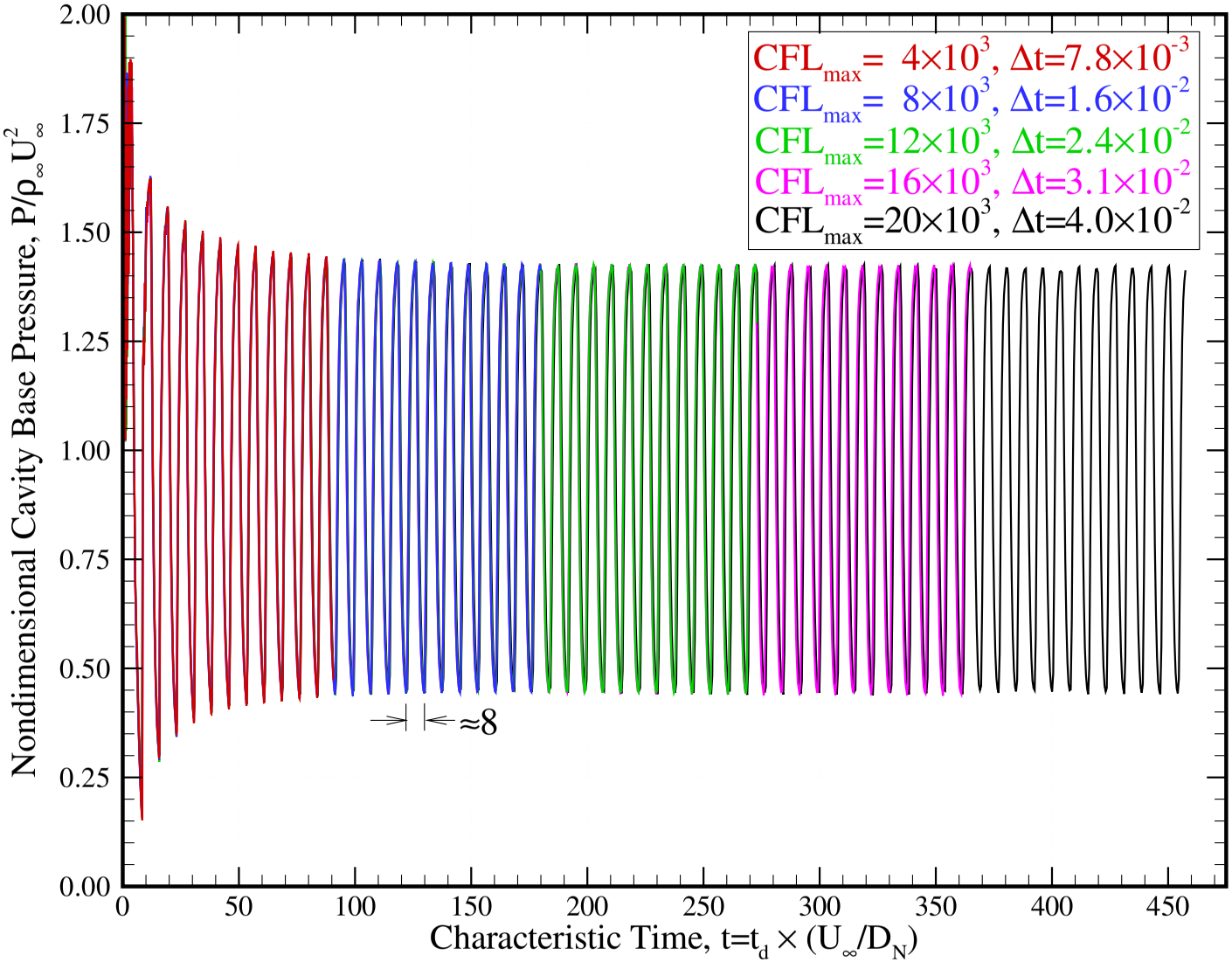

Background

- A sharp 25°–55° double cone was tested in N_2 at CUBRC
- It was discovered that freestream vibrational nonequilibrium must be properly modeled for CFD to match experiment [15]
- The AEDC Hypervelocity Wind Tunnel No. 9 also uses N_2 as its test gas
- A series of tests were conducted at AEDC using the same model to investigate the presence of vibrational nonequilibrium in the freestream [16]

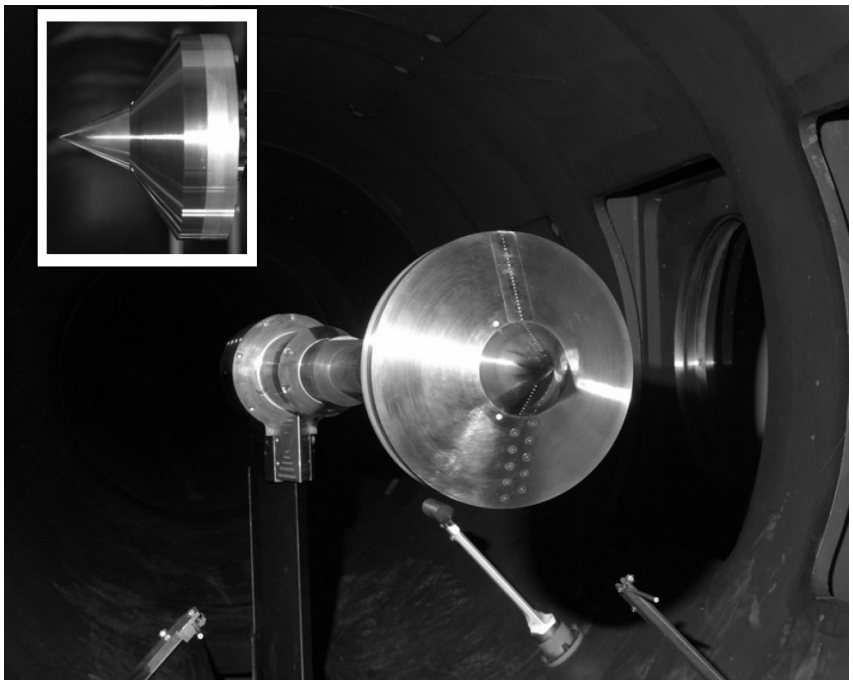

Observations

- Four Reynolds numbers were tested in the nominally Mach 14 nozzle
- No appreciable vibrational nonequilibrium effects observed
- Highly unsteady flow observed for *all* Reynolds numbers tested
- For a uniform freestream, CFD predicts steady flow for the two lowest Reynolds numbers

Run	2890	2891	2893	2894	
M_∞	13.6	13.17	12.73	12.63	
Re_D	1.12×10^6	4.11×10^5	8.44×10^4	5.86×10^4	
ρ_∞	7.81×10^{-3}	2.96×10^{-3}	5.90×10^{-4}	3.98×10^{-4}	kg/m^3
U_∞	2006.6	1949.8	1763.5	1682.6	m/sec
T_∞	52.3	52.7	46.1	42.7	K

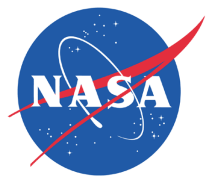

Steady states, runs 2893 and 2894

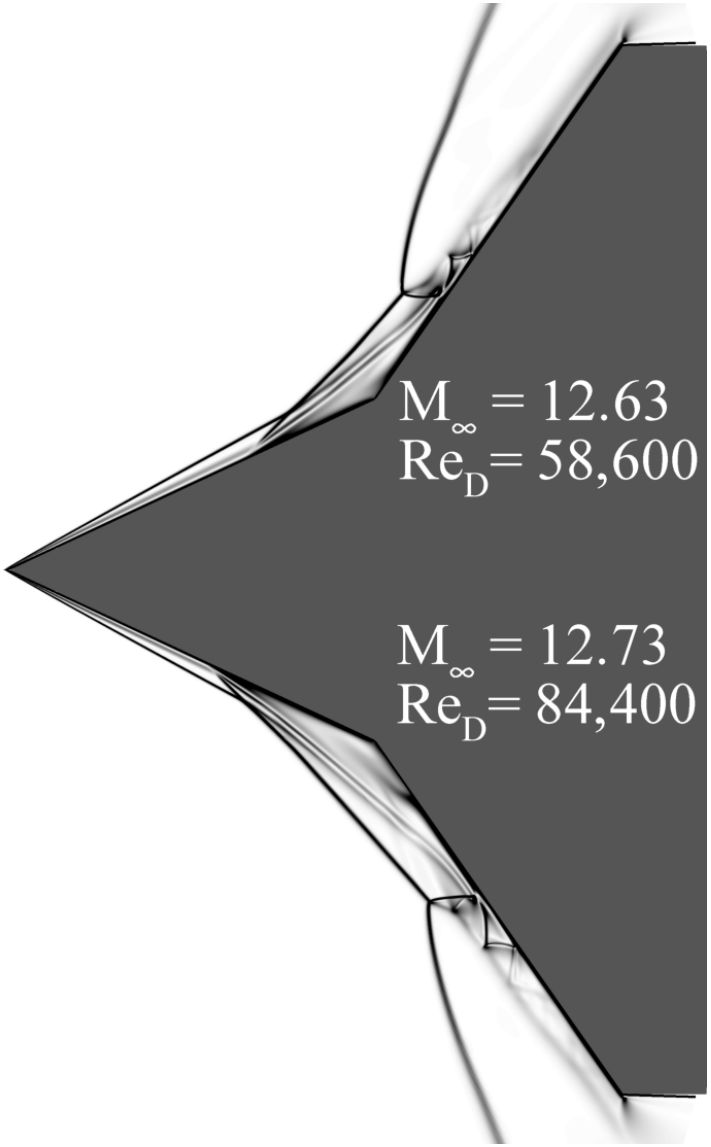

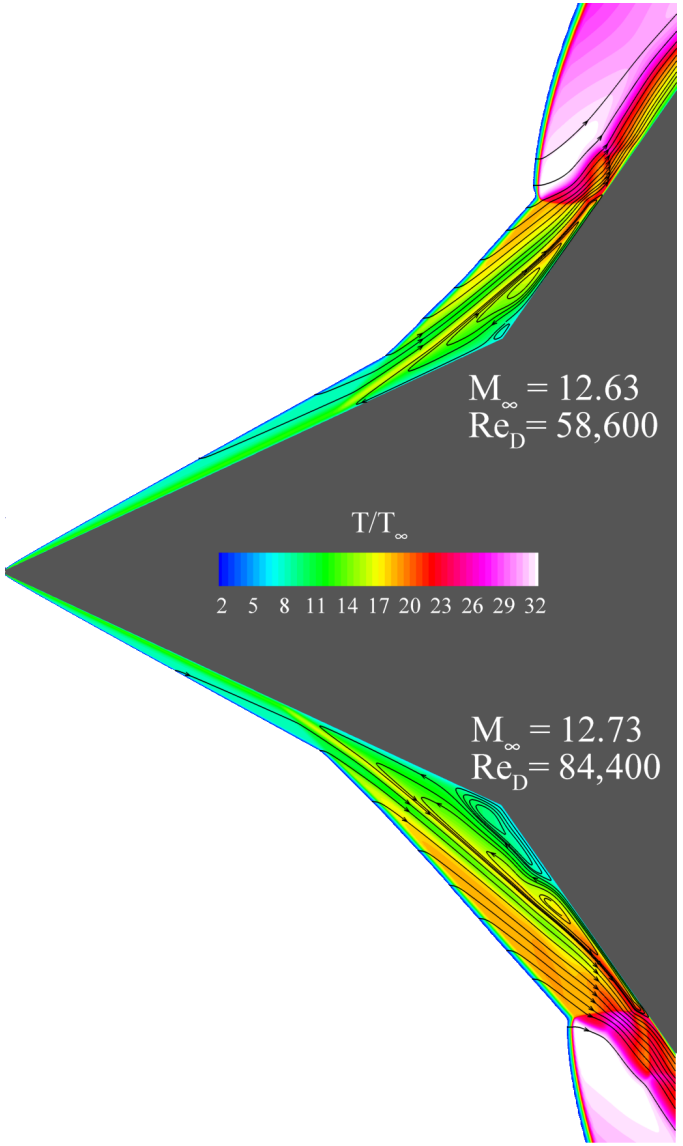

Time Convergence, run 2894

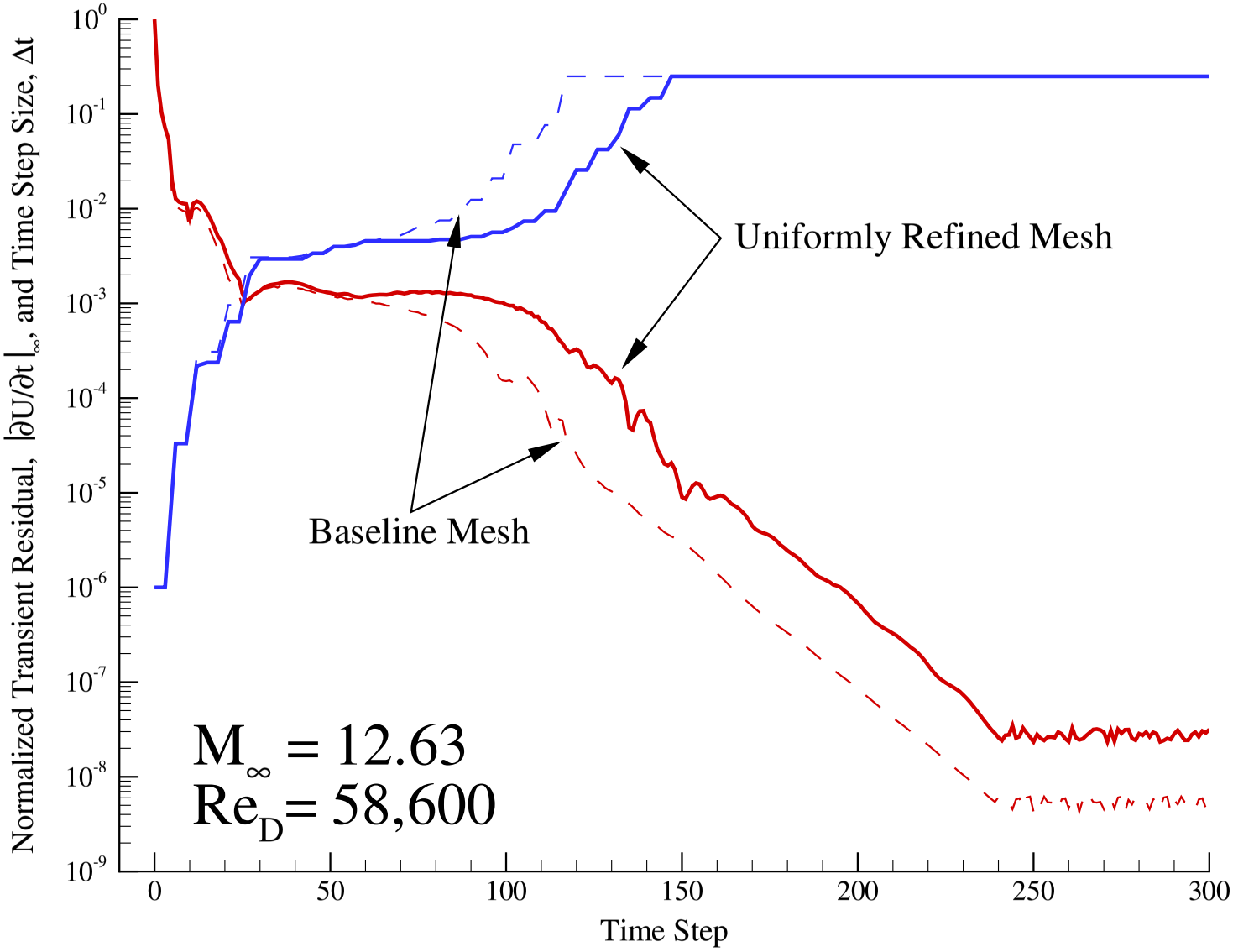

AEDC Sharp Double Cone

High speed schlieren, run 2890

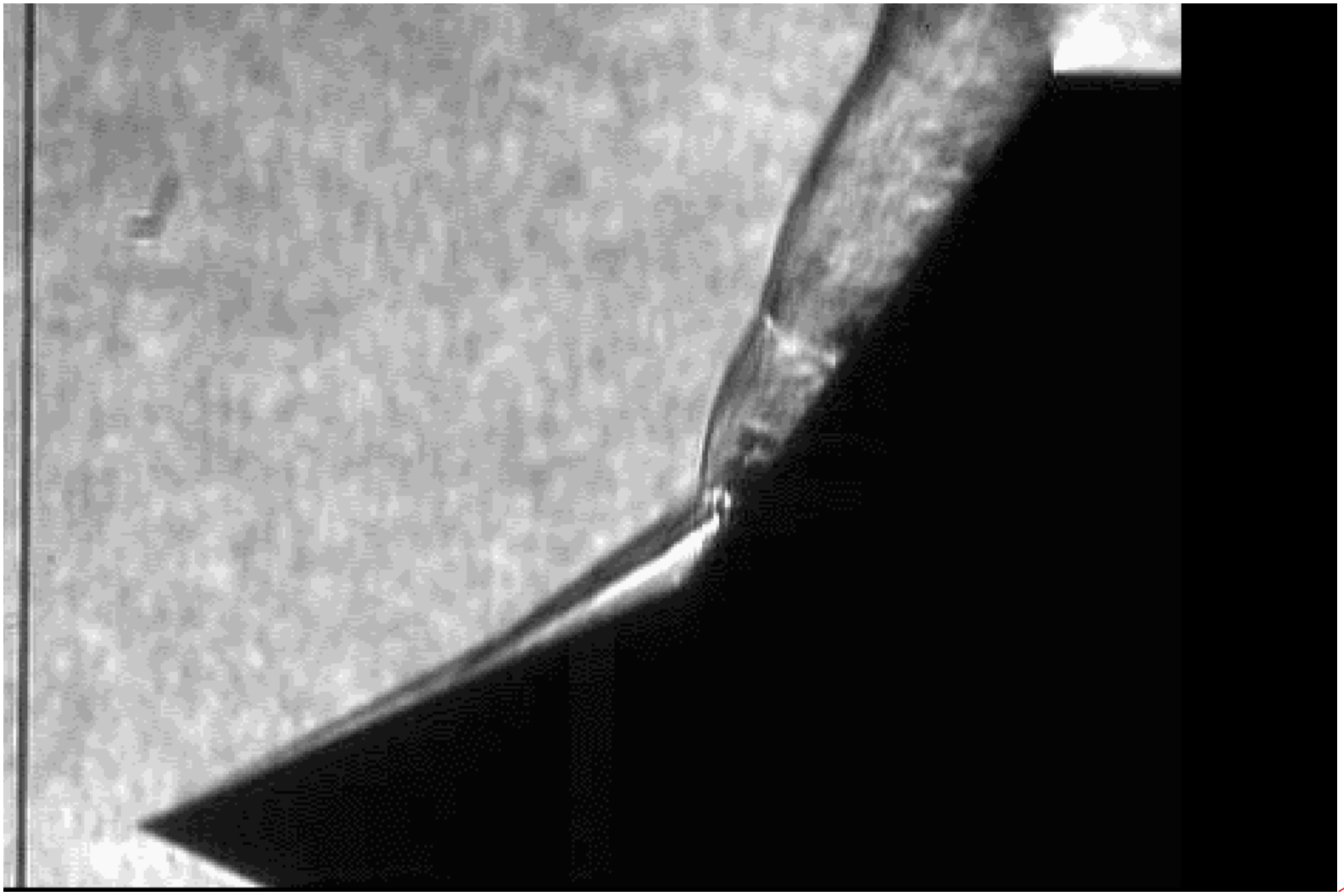

Computed schlieren, run 2890

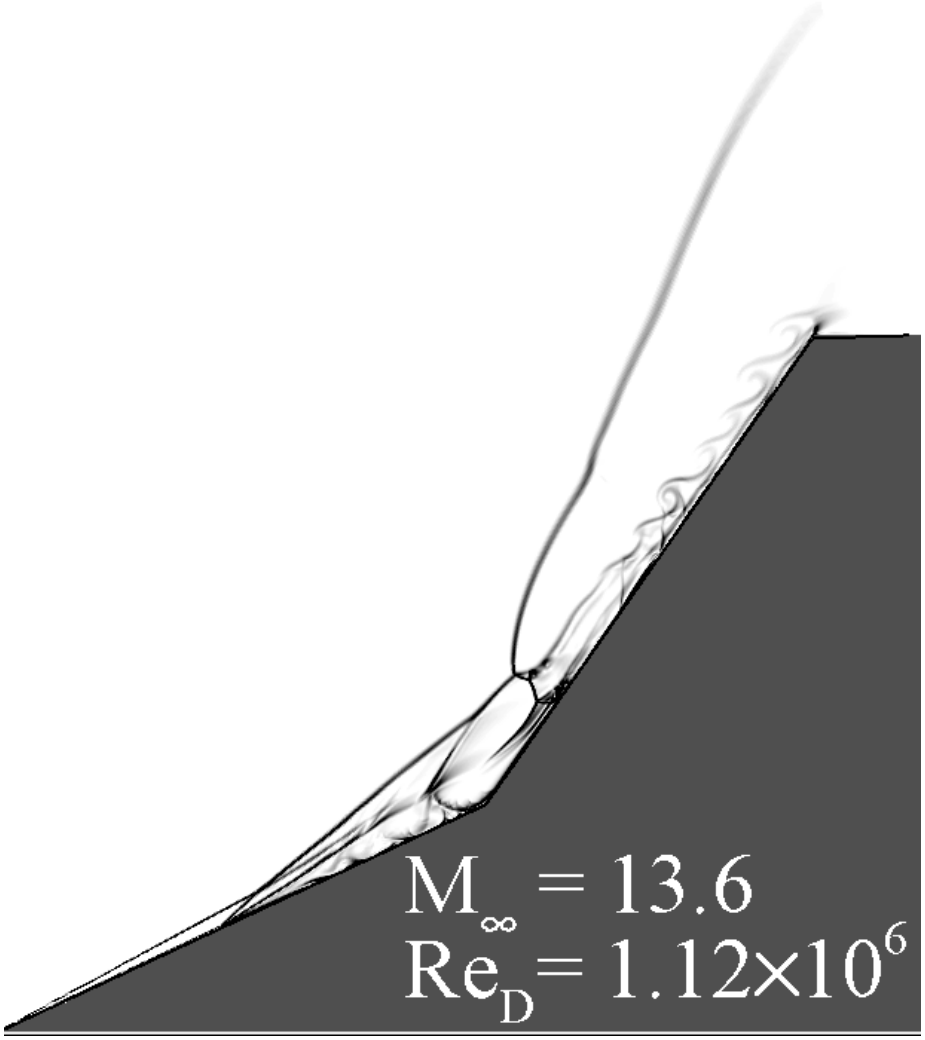

Possible Mechanism for Observed Unsteadiness

- For a uniform inflow, CFD converges to a steady–state for the two lowest Reynolds numbers tested
- This is in contrast to the experimental results
- My conjecture is that freestream noise drives the unsteady behavior at these low Reynolds number
- Remaining analysis is focused on testing this theory

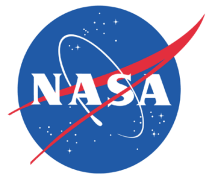

Noise Characterization [17]

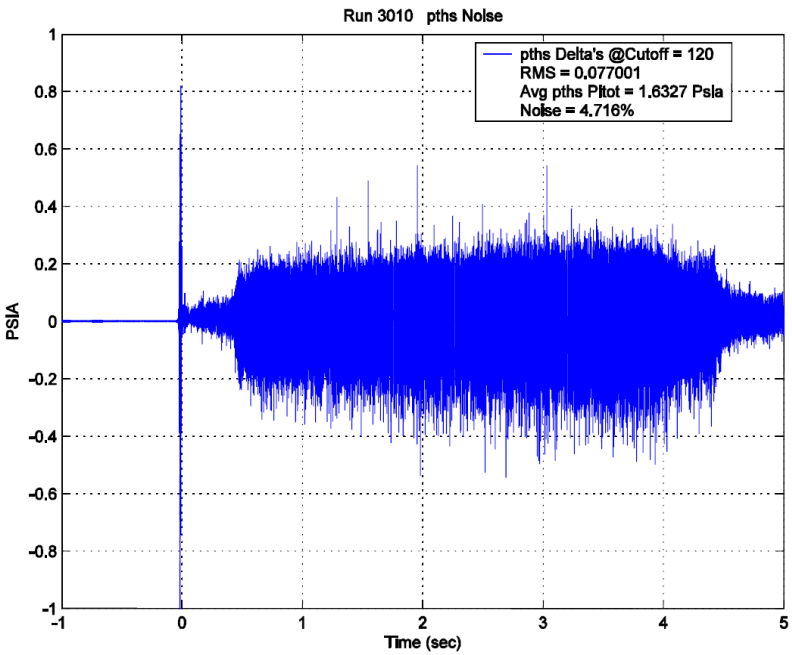

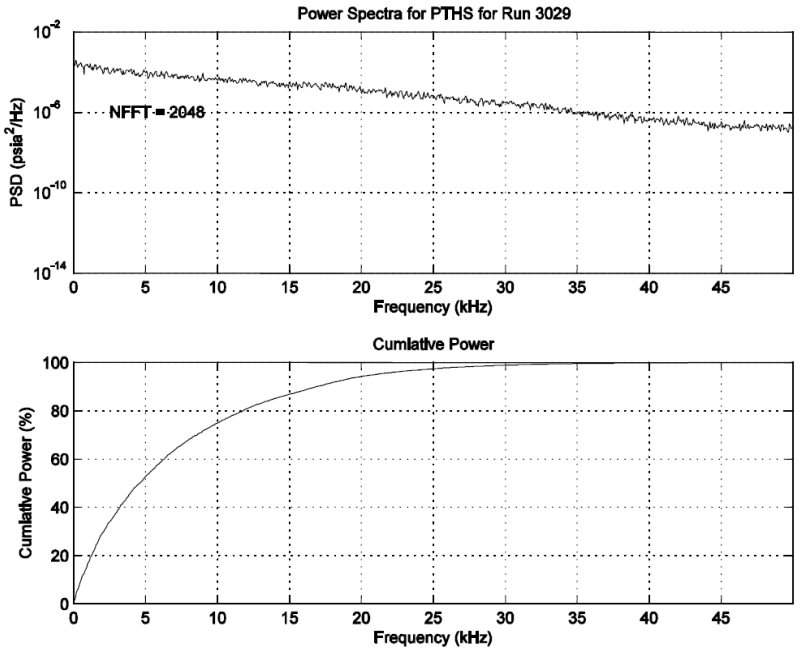

Noise Characterization [17]

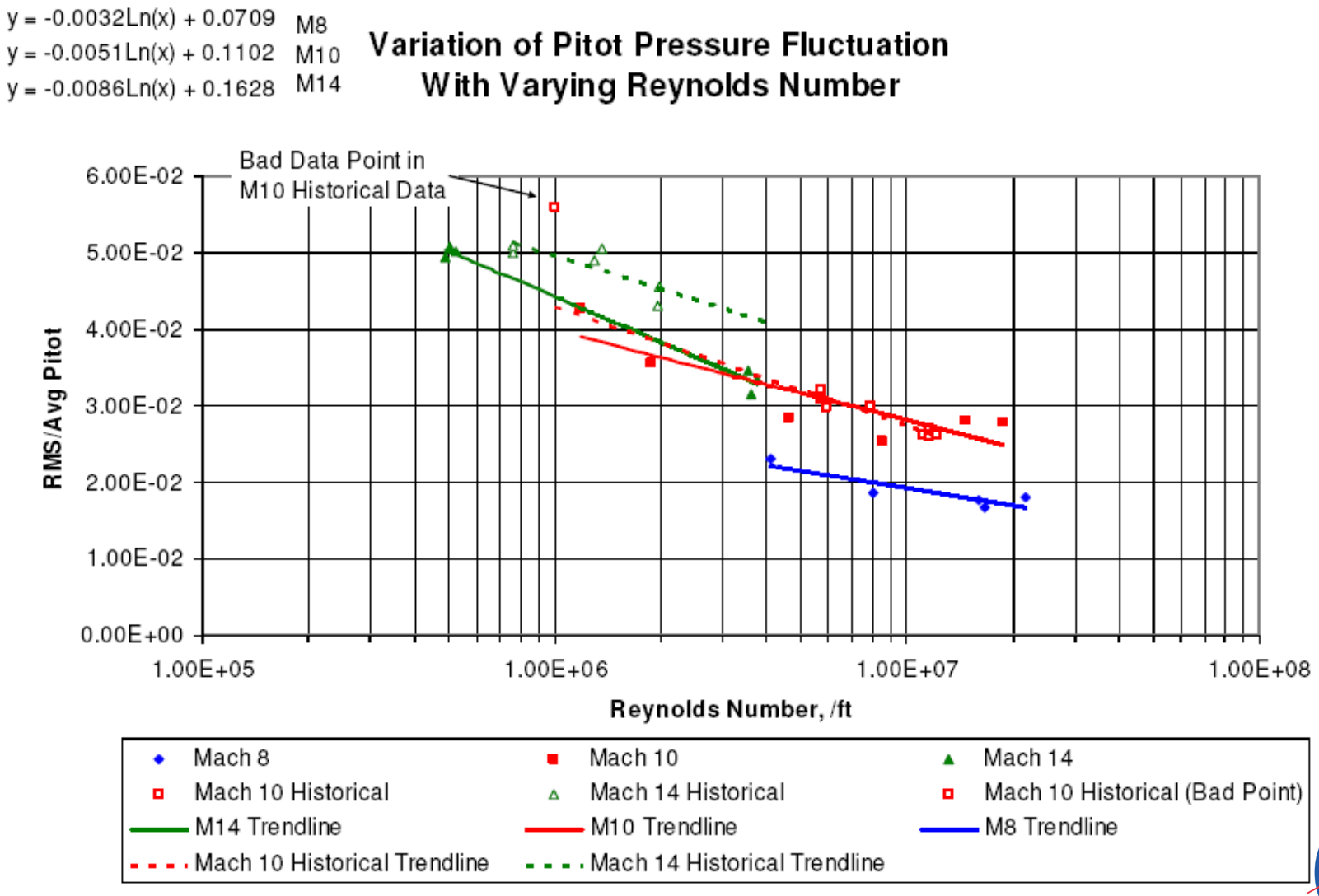

Results – Flowfield

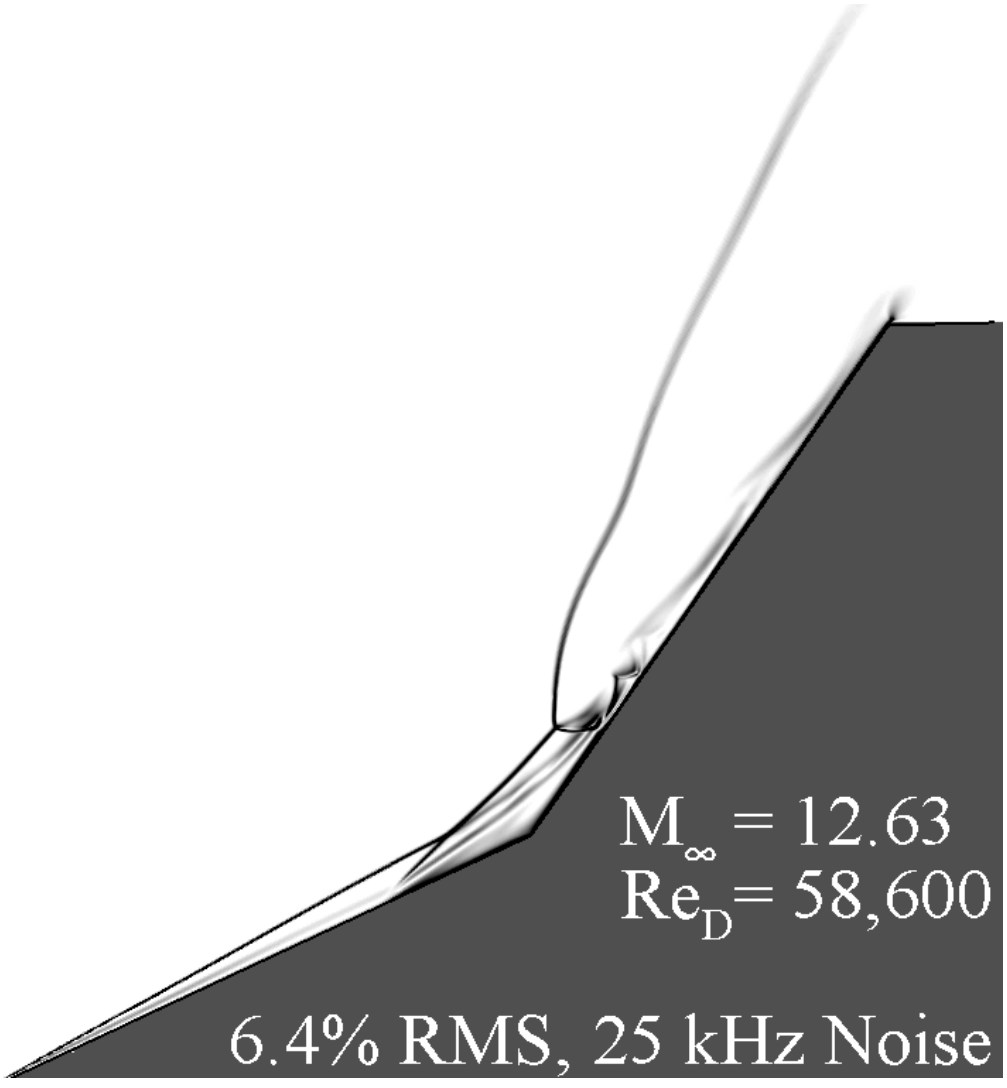

Results – Surface Pressure

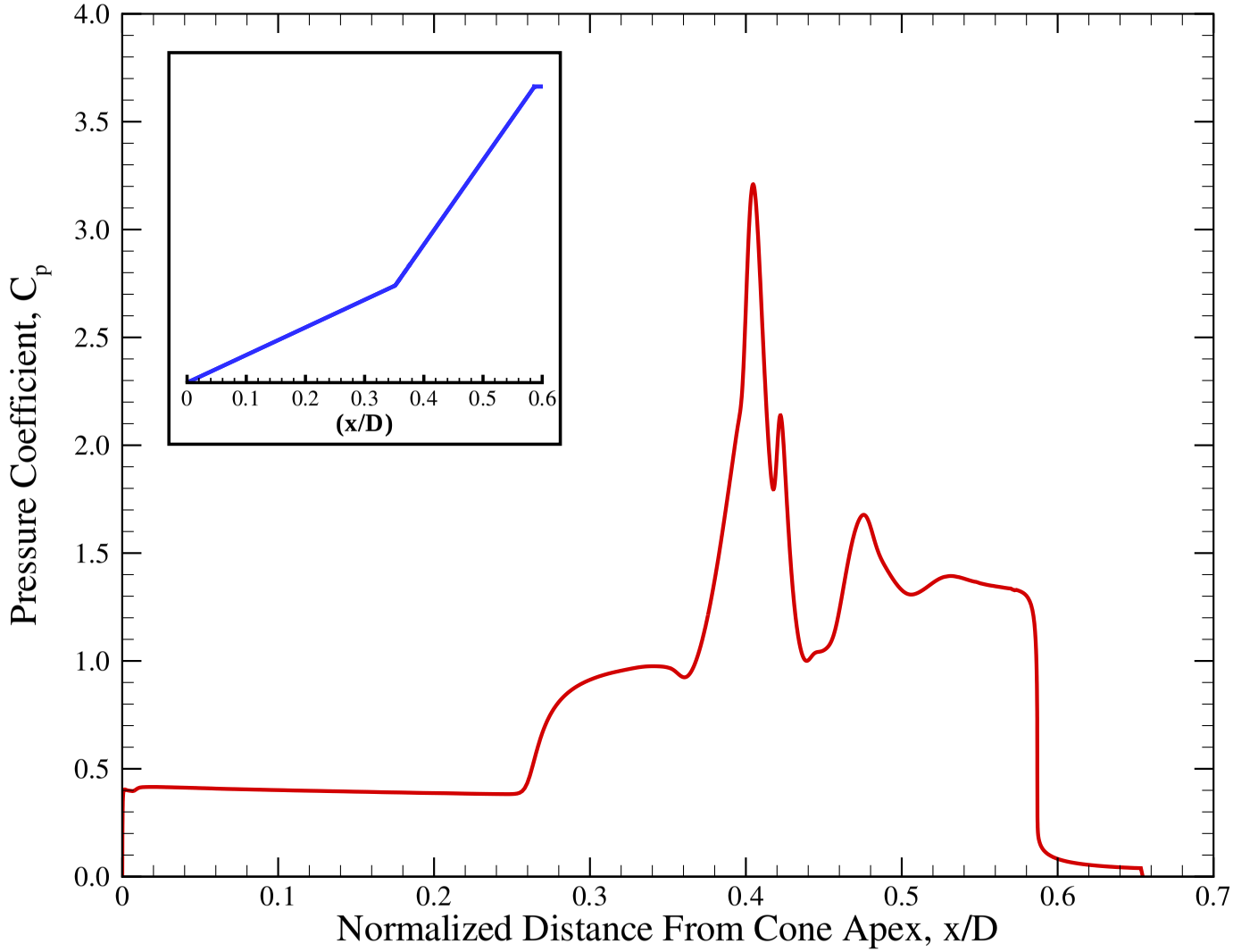

AEDC Sharp Double Cone

25 kHz, 6% RMS Pitot Pressure Fluctuation

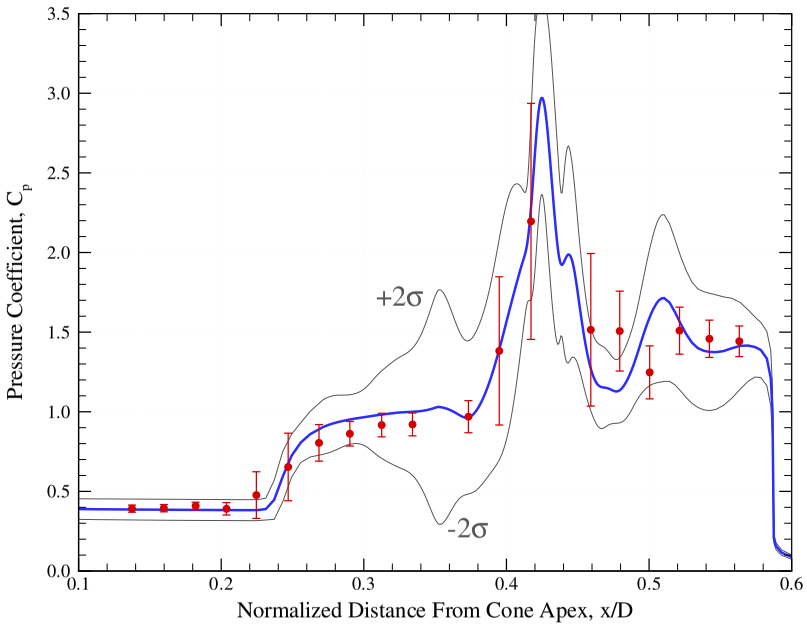

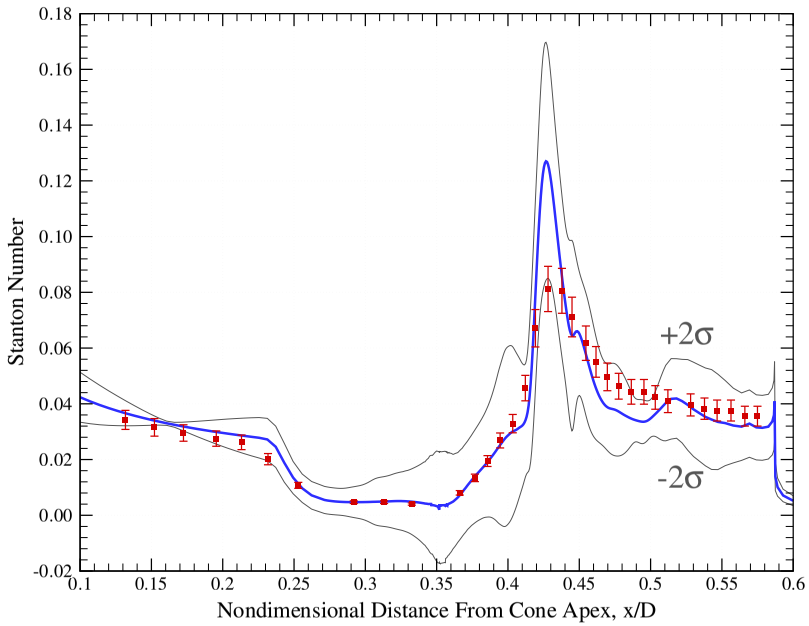

Frequency Influence

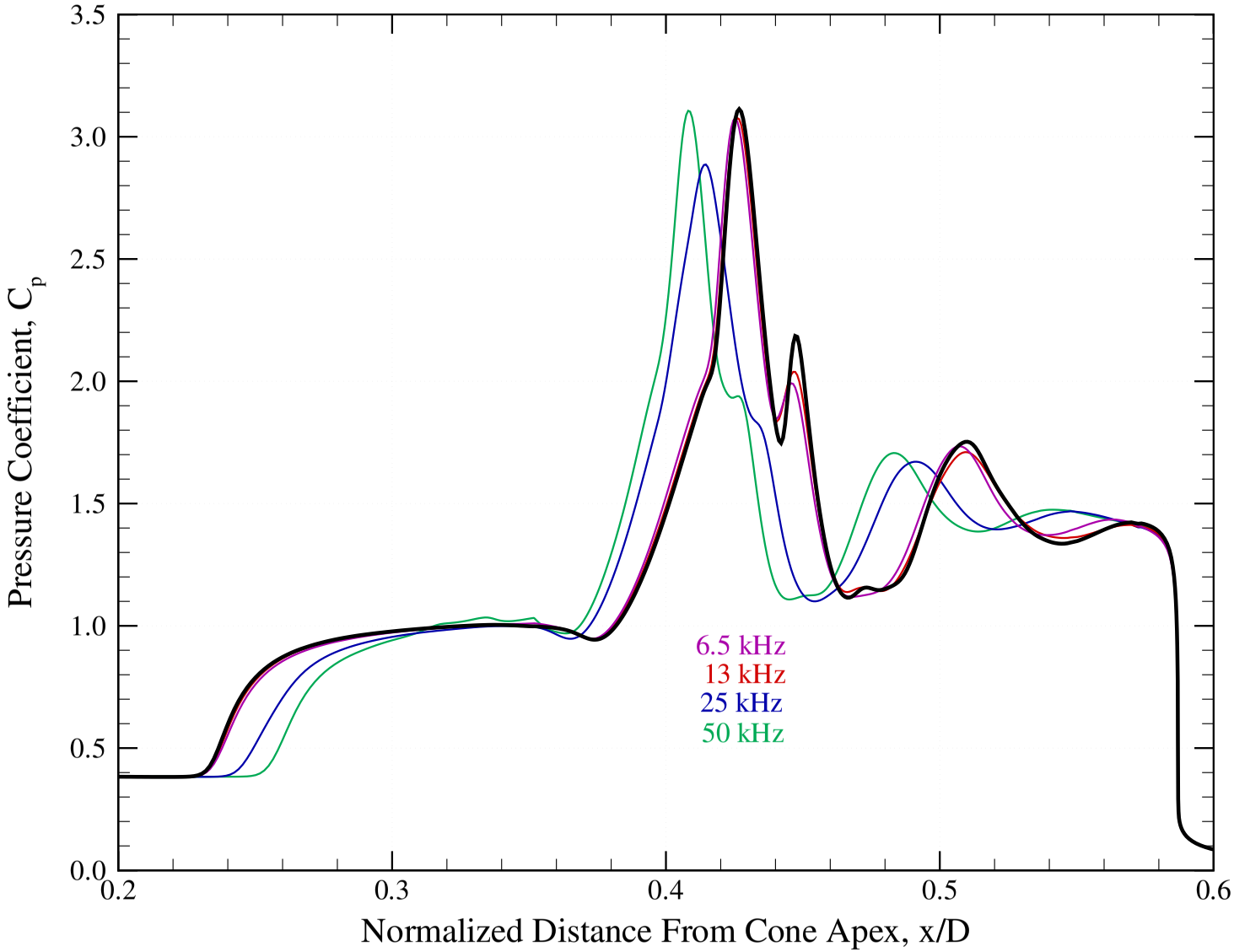

[1] J. C. Tannehill, D. A. Anderson, and R. H. Pletcher.
Computational Fluid Mechanics and Heat Transfer.
Taylor & Francis, Washington, D.C., 2nd edition, 1997.

[2] Ronald L. Panton.
Incompressible Flow.
John Wiley & Sons, 2nd edition, 1996.

[3] G. Hauke and T. J. R. Hughes.
A comparative study of different sets of variables for solving compressible and incompressible flows.
Computer Methods in Applied Mechanics and Engineering, 153:1–44, 1998.

[4] G. J. LeBeau.
The finite element computation of compressible flows.
Master's thesis, The University of Minnesota, 1990.

[5] S. K. Aliabadi.
Parallel Finite Element Computations in Aerospace Applications.
PhD thesis, The University of Minnesota, 1994.

[6] S. K. Aliabadi and T. E. Tezduyar.
Parallel Fluid Dynamics Computations in Aerospace Applications.
International Journal for Numerical Methods in Fluids, 21:783–805, 1995.

[7] T. J. R. Hughes and M. Mallet.
A new finite element formulation for computational fluid dynamics: IV. a discontinuity operator for multidimensional advective–diffusive systems.
Computer Methods in Applied Mechanics and Engineering, 58:329–336, 1986.

[8] Farzin Shakib, Thomas J. R. Hughes, and Zdeněk Johan.
A new finite element formulation for computational fluid dynamics: X. the compressible Euler and Navier–Stokes equations.
Computer Methods in Applied Mechanics and Engineering, 89:141–219, 1991.

[9] L. Catabriga and A. L. G. A. Coutinho.
Improving convergence to steady state of implicit SUPG solution of Euler equations.
Communications in Numerical Methods in Engineering, 18(5):345–353, May 2002.

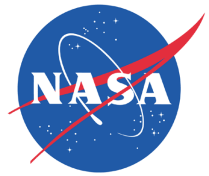

[10] B. Edney.
Anomalous heat transfer and pressure distributions on blunt bodies at hypersonic speeds in the presence of an impinging shock.
Technical report, Flygtekniska Försöksanstalten (the Aeronautical Research Institute of Sweden), Stockholm, 1968.

[11] T. Pot, B. Chanetz, M. Lefebvre, and P. Bouchardy.
Fundamental study of shock/shock interference in low density flow.
21st International Symposium on Rarefied Gas Dynamics, 1998.

[12] W. A. Engblom and D. B. Goldstein.
Nose-tip surface heat reduction mechanism.
34th AIAA Aerospace Sciences Meeting and Exhibit, AIAA Paper 1996-354, January 1996.

[13] Sidra I. Silton and David B. Goldstein.
Ablation onset in unsteady hypersonic flow about nose tip with cavity.
Journal of Thermophysics and Heat Transfer, 14(3):421–434, July–September 2000.

[14] W. A. Engblom, D. B. Goldstein, D. Landoon, and S. P. Schneider.
Fluid dynamics of hypersonic forward-facing cavity flow.
34th AIAA Aerospace Sciences Meeting and Exhibit, AIAA Paper 1996-667, January 1996.

[15] Ioannis Nompelis, Graham V. Candler, and Michael S. Holden.
Effect of Vibrational Nonequilibrium on Hypersonic Double-Cone Experiments.
AIAA Journal, 41(11):2162–2169, November 2003.

[16] Joseph J. Coblish, Michael S. Smith, Terrell Hand, Graham V. Candler, and Ioannis Nompelis.
Double-Cone Experiment and Numerical Analysis at AEDC Hypervelocity Wind Tunnel No. 9.
43rd AIAA Aerospace Sciences Meeting and Exhibit, AIAA Paper 2005-0902, January 2005.

[17] J. McNalley.
Pitot Noise Measurement During FY06 NASA MSL Test.
Arnold Engineering Delvelopment Center Memorandum, September 2006.